Observations, Simulations, and Analysis of Nonstationary Trapped Lee Waves

F. MARTIN RALPH AND PAUL J. NEIMAN

NOAA/ERL Environmental Technology Laboratory, Boulder, Colorado

TEDDIE L. KELLER

NCAR/Research Applications Program, Boulder, Colorado

DAVID LEVINSON AND LEN FEDOR

CIRES, University of Colorado/NOAA, Boulder, Colorado

(Manuscript received 1 May 1996, in final form 11 November 1996)

ABSTRACT

Although considerable understanding of mountain waves has been gained with the aid of the steady-state assumption, it is clear that mountain waves evolve over time. Group velocity arguments indicate that this evolution can occur in less than 1 h. This study uses observations of trapped lee waves to measure the rate at which their horizontal wavelengths change, including a detailed analysis of two events in which such changes are clearly documented. In one case, Doppler lidar observations show a steady increase in horizontal wavelength of 6% h^{-1} over 4 h and clearly illustrates the relationship between the wave clouds and wave motions. In a second case, visible satellite imagery reveals an increase in wavelength of 14% h^{-1}, which is related to temporal changes in vertical air motions measured by wind profilers within the wave field. Hourly vertical profiles of wind and virtual temperature measured by radio acoustic sounding systems (RASS) and wind profilers reveal important changes in the wave environment. These data were used to initialize a two-dimensional nonlinear nonhydrostatic numerical model with soundings representing five times over 8 h. Each simulation produced trapped lee waves. The simulations support the conclusion that the observed increase in wavelength resulted from changes in the wave environment. Uncertainty in the predicted wavelength due to using measurements within the trapped lee waves as initial conditions is shown to be small in this case. The wind profiler and RASS measurement accuracies are adequate to measure changes leading to trapped lee wave nonstationarity.

The results from these two case studies are combined with evidence of nonstationarity found in earlier papers and additional events documented here using visible satellite imagery. These 24 observations of nonstationarity indicate that the horizontal wavelength of trapped lee waves can change by as much as 30% h^{-1}. The average of all events, most of which occurred at midday, is a 9% h^{-1} temporal increase. It is suggested that the deepening of the mixed layer thins the elevated stable layer that is a key part of the waveguide and that this thinning causes the systematic temporal increase of the horizontal wavelength.

While this study focused on trapped lee waves, it can be inferred that vertically propagating waves can also change significantly over a few hours. Because aircraft measurements of vertical momentum flux profiles typically require 2–5 h to complete, and stationarity is required over that time, it is recommended that steadiness should be measured rather than assumed in such studies.

1. Introduction

Under certain conditions, airflow over a mountain can force gravity waves that are trapped vertically, creating a train of waves in the lee of the mountain. These waves can contribute to mountain wave drag by redistributing the drag well downstream of the mountain as wave energy ultimately leaks upward (e.g., Keller 1994). The behavior of such trapped lee waves has been reviewed by Queney et al. (1960), Smith (1979), Atkinson (1981), Lilly (1983), Durran (1986), and Wurtele et al. (1996). Much understanding of this phenomenon has been gained through treatment of trapped lee waves as a steady-state problem both in early studies (e.g., Queney 1948; Scorer 1949; Long 1955; Queney et al. 1960; Sawyer 1962) and in more recent analyses (e.g., Sharman and Wurtele 1983; Mitchell et al. 1990; Shutts and Broad 1993; Keller 1994).

Although it is clear that mountain waves must evolve over time in response to changing upstream conditions (e.g., Bell 1975; Bannon and Zehnder 1985; Lott and Teitelbaum 1993; L. Nance and D. Durran 1996a, manuscript submitted to *J. Atmos. Sci.*, hereafter referred to

Corresponding author address: Dr. F. Martin Ralph, NOAA/ERL/ETL, mail code R/E/ET7, 325 Broadway, Boulder, CO 80303.
E-mail: fralph@etl.noaa.gov

as ND96a), no systematic observational assessment of temporal changes in mountain waves has been presented. Some of the earliest field observations, however, did refer to unsteady behavior, as summarized in Queney et al. (1960). One conclusion from the Sierra Wave Project (Holmboe and Klieforth 1957) was that a steady lengthening of the wavelength sometimes occurred during the day. Similarly, studies in the French Alps reported a decrease in wave amplitude and an increase in wavelength in the afternoon and speculated that the changes were caused by diurnal heating (Queney et al. 1960; Gerbier and Berenger 1961). Förchtgott (1957) noticed from sailplane observations that lee wave clouds and their associated rotors would frequently move an appreciable fraction of a wavelength downstream over several minutes and then jump back upstream toward the mountains over a matter of seconds. Reynolds et al. (1968) reported that more than 25% of more than 100 mountain wave events observed with constant volume balloons exhibited ''complex wave patterns,'' defined as a series of waves in horizontal succession displaying variable wavelengths and amplitudes, and suggested that this type of wave pattern resulted from changes in wavelength and amplitude over time. Vergeiner and Lilly (1970), using sequential flights of constant-level balloons and aircraft over the Colorado Rocky Mountains, noted that ''the nonstationarity of many flow features is inescapable and poses serious problems for data evaluation and theory.'' Nonstationary trapped waves were clearly documented in three of the events they presented, and it was concluded that the wave pattern can be very sensitive to small changes in upstream conditions. (The term ''nonstationary'' is used here to represent temporal changes in the horizontal wavelength of the trapped lee waves.) Starr and Browning (1972) presented remarkably clear observations of lee waves using a 10-cm radar, including one event in which distinct temporal changes occurred over a period of about 1 h. Variations on this timescale have also been found in both the sign and amplitude of vertical motions observed by clear-air radar wind profilers in the lee of mountains at many sites around the world (Ecklund et al. 1982; Balsley and Carter 1989; Sato 1990; Ralph et al. 1992; Prichard et al. 1995; Worthington and Thomas 1996). Based on conclusions in Ralph et al. (1992) that such variability is indicative of mountain wave nonstationarity, it appears that nonstationarity is common, as was also suggested by Reynolds et al. (1968). This conclusion is consistent with earlier studies in which the sensitivity of the trapped wavelength to small changes in upstream conditions is well brought out using idealized wind and static stability profiles to show the wavelength dependency of trapped lee waves on upstream conditions (Corby and Wallington 1956; Palm and Foldvik 1960; Foldvik 1962).

In a study closely related to ours, Mitchell et al. (1990) used linear theory to determine the trapped lee-wave structure at three different times, each 12 h apart. The change in the trapped wavelength calculated using the three soundings was then shown to be consistent with the change inferred from a satellite image that showed a longer wavelength (15.4 km) downstream of a shorter wavelength (10.0 km). Although the soundings used were 12 h apart, the data imply that the change occurred over less than 1 h.

Based on the observations summarized above [constant-pressure balloons (Reynolds et al. 1968; Vergeiner and Lilly 1970), 10-cm radar (Starr and Browning 1972), radar wind profilers (Ralph et al. 1992), and satellite (Mitchell et al. (1990)], there appears to be ample evidence that the timescale for wavelength adjustment can be less than 1 h. This is consistent with estimates based on the time required to modify one horizontal wavelength, assuming downstream propagation at the group velocity, as described in Queney et al. (1960), where it was concluded that this timescale is on the order of 10–30 min. Lott and Teitelbaum (1993) used a similar argument based on the time required to adjust one vertical wavelength on the order of the depth of the troposphere to conclude that the wavelength change could occur in less than 1 h for typical trapped wavelengths. The most direct determination of the timescale for adjustment in trapped waves can be found in the nonlinear numerical modeling study of Foldvik and Wurtele (1967), in which the temporal development of mountain waves was studied by suddenly introducing a mountain into a steady horizontal flow with wave trapping characteristics. From their results it can be shown that the first wave downstream from the mountain reached more than 90% of its predicted amplitude within 45 min. Recently, ND96a found similar timescales in numerical simulations of trapped lee waves using idealized temporally varying upstream conditions.

In addition to the fact that nonstationarity can result from temporal changes in upstream conditions, L. Nance and D. Durran (1996b, manuscript submitted to *J. Atmos. Sci.*, hereafter referred to as ND96b) used nonlinear theory and a nonlinear two-dimensional numerical model to suggest that trapped lee waves can become nonstationary due to nonlinear wave–wave interactions even when upstream conditions are steady. Some support for this hypothesis is also found in simulations by Satomura and Bougeault (1994).

Although the studies reviewed above suggest that temporal variations of trapped lee waves can occur on a timescale of 1 h or less, the range and average of such changes have not been established from observations. This paper intends to synthesize the evidence of nonstationarity found in earlier studies with the observations presented here of two events where nonstationarity is precisely measured and to quantify the rate at which the wavelength of trapped lee waves changes. In the first case study, a Doppler lidar (Post and Cupp 1990) is used to document the position of a train of three to four lee waves over 4 h. In a second case study, satellite imagery is combined with frequent ($<$1 h) profiles of

the horizontal wind from a 404-MHz wind profiler (Ralph et al. 1995) and of virtual temperature from radio acoustic sounding systems (RASS) (May et al. 1990) to relate changes in the wave environment to satellite-observed changes in horizontal wavelength. The frequent wind and temperature profiles are then used to initialize a two-dimensional nonlinear numerical model (Pihos and Wurtele 1981; Sharman et al. 1988) at five times during 8 h of the evolution of the trapped waves, which extended up to 12 wavelengths downstream. This tests the hypothesis that changing upstream conditions caused the observed wavelength changes and more clearly documents that such changes can occur on this short timescale. Recent work by Shutts and Broad (1993), in which serial balloon ascents were used to successfully validate simulations from a three-dimensional primitive equation model that had reached a quasi-steady state, illustrates the reliability of predictions of trapped lee waves, when timely upstream conditions are used. A summary of 24 observed cases of nonstationarity, 15 of which are from sequences of visible satellite images, is then used to quantify the speed at which wavelength changes occur. The use of the steady-state assumption in observational studies of mountain wave drag, in which the waves are assumed stationary over the 2–5 h typically required to make the aircraft observations, is addressed in light of the results shown here.

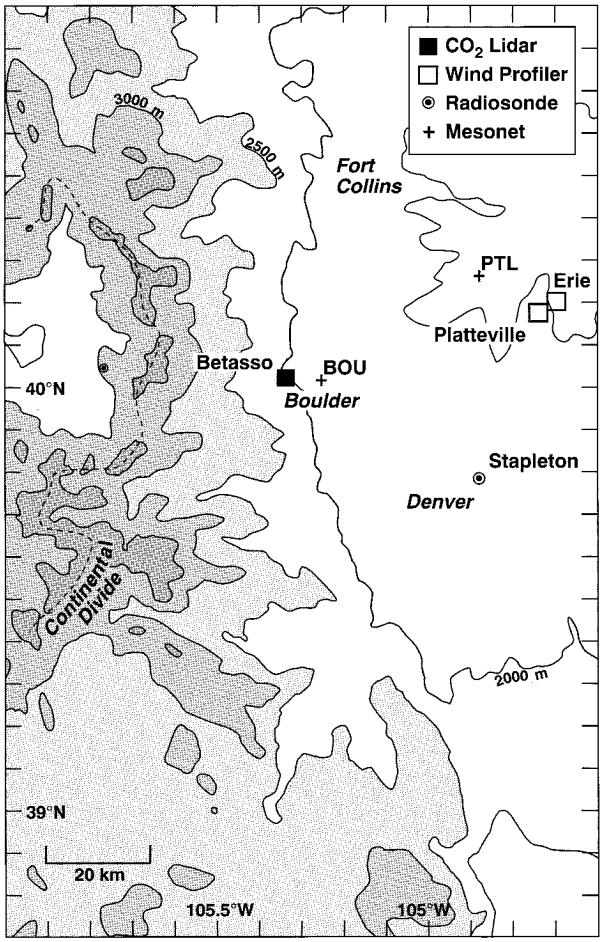

FIG. 1. Base map showing the positions of the instruments relative to the topography of northeastern Colorado. The ceilometer, radiometer, and visual cloud-base measurements were made from the rawinsonde site. The dashed line marks the Continental Divide. Major cities are marked.

2. The observing systems and local terrain

a. Background

This paper presents observations from a variety of remote sensors deployed along the eastern edge of the Colorado Rocky Mountains near Boulder, Colorado. Figure 1 shows the locations of the instruments and the surrounding terrain. The data are used to document the behavior of trapped lee waves in two detailed case studies on 2 February 1987 and 8 April 1992. In addition, several cases based solely on visible satellite imagery are summarized. Because of the variety of instruments used in this study, a brief summary of their characteristics is given below and in Table 1.

b. Radar wind profilers

Wind profilers provide vertical profiles of horizontal and vertical motions every few minutes above a fixed site using backscatter from variations in the atmospheric index of refraction or from hydrometeors (e.g., Gage 1990). Past studies cited in section 1 have established the utility of wind profiler measurements in documenting episodes of mountain waves, the temporal variability of such waves, and their vertical structure. The horizontal winds are measured with an accuracy of ± 1.3 m s^{-1} (Strauch et al. 1987; Wuertz et al. 1988). Several findings suggest that the vertical velocity measurements are rather accurate: an indirect estimate for VHF [very high frequency (30–300 MHz)] radars (Ralph 1991), an intercomparison between collocated UHF [ultrahigh frequency (300–3000 MHz)] and VHF radars (McAfee et al. 1994), the improvement of RASS accuracies (Moran and Strauch 1994), and good agreement between mountain wave theory and observations (Ralph et al. 1992; Prichard et al. 1995; Worthington and Thomas 1996). Both the indirect methods of Ralph (1991) and the more direct instrument comparison approach of McAfee et al. (1994) suggest an accuracy of roughly ± 0.1 m s^{-1}.

The case study of 8 April 1992 presented here benefits from the availability of both 50- and 404-MHz profilers at Platteville and a 404-MHz profiler sited nearby at Erie, Colorado, that was devoted to RASS measurements. The 50-MHz radar, which is relatively insensitive to hydrometeors, was switched to a special mode at 2041 UTC 8 April 1992, partway through the wave event, to provide better temporal and vertical resolution of tem-

TABLE 1. Key instrumentation in Colorado.

Instrument	Variables measured	Site name	Latitude (°N)	Longitude (°W)	Altitude (m MSL)
CO_2 Doppler lidar	Radial velocity Backscatter intensity	Betasso	40.01	105.34	1945
50-MHz profiler and RASS	Horizontal wind Virtual temperature Vertical velocity	Platteville	40.18	104.73	1524
404-MHz profiler and RASS	Horizontal wind Virtual temperature Vertical velocity	Platteville	40.18	104.73	1524
404-MHz RASS	Virtual temperature	Erie	40.20	104.70	1503
Rawinsonde	Horizontal wind Temperature Water vapor	Stapleton	39.77	104.88	1611

perature and vertical velocity at the expense of horizontal wind measurements. Before (after) it was switched to the new parameters, a 9-μs (3-μs) pulselength was used to measure vertical velocity at 3.3-min (1-min) intervals and 900-m (450-m) gate spacing from 3.2 km (3.8 km) above mean sea level (MSL) to 10–18 km MSL. (Henceforth, all altitudes are MSL unless otherwise noted.) The 404-MHz radar at Platteville, which is part of the National Oceanic and Atmospheric Administration's (NOAA) wind profiler network described in Barth et al. (1994) and Ralph et al. (1995), used 250-m vertical gate spacing starting at 2.0 km and measured vertical and horizontal motions using three beams. The hourly consensus-averaged horizontal winds were smoothed using one pass of a temporal Hann filter to reduce the effects of $2\Delta t$ (= 2 h) variations. A total of about 15 points were interpolated, before 2000 UTC and between 7.5 and 9 km, where the radar signal was too weak to obtain meaningful measurements. Because the 404-MHz radar is sensitive to hydrometeors (e.g., Ralph 1995), the radar-observed vertical velocities must be interpreted with caution in cloudy or precipitating regions. Because the horizontal wavelength of the gravity waves (16–20 km) greatly exceeds the beamwidths and the beam spacing, which are less than 1 and 2 km, respectively, at 10 km, errors in the radial velocity and in the retrieved horizontal winds due to gravity wave–induced variations in the wind field should be small (Ralph et al. 1992).

c. Radio acoustic sounding systems

A RASS measures the vertical profile of virtual temperature T_v by using a wind profiler to track the propagation of an acoustic wave transmitted vertically by a nearby acoustic source (May et al. 1990). For the 8 April 1992 case study both the 404- and 50-MHz profilers at Platteville included RASS systems, and another 404-MHz radar located nearby at Erie measured T_v with RASS every 30 min.

As established by Moran and Strauch (1994), the accuracy of the T_v retrieval from VHF radars is improved substantially from ± 1.6°C to ± 0.9°C after correcting the vertical propagation of the acoustic wave for advection by the local vertical air motion, both of which are measured simultaneously. Making this correction is particularly important when the vertical velocities are large, as in the situations studied here. The 50-MHz RASS measured the T_v profile once every 1 min for 5–6 min. These samples were then used to create a 6-min average that is assumed to represent that hour. Beginning at 2041 UTC, the 5–6-min samples were gathered three times per hour, and the 1-h-average T_v profiles were calculated with a consensus-averaging technique using all samples during that hour. The Erie 404-MHz RASS measured the T_v profile once every minute for 5–6 min, every half hour. These data were then consensus-averaged to create a T_v measurement representing that hour. The Platteville 404-MHz RASS data were excluded from the current analysis because the RASS system was still under development.

Data from the 50-MHz RASS and the Erie 404-MHz RASS, each averaged for 1 h, were combined with surface observations from a nearby site (the Platteville mesonet site) to show the evolution of the thermodynamic structure from the ground to about 9 km MSL at hourly intervals. The pressure–height relationship, which is required for calculation of potential temperature, was determined from the surface and RASS data up to its upper limit and then from the Denver rawinsonde ascents. It should be noted that the maximum range of the RASS T_v retrievals is limited by acoustic attenuation, strong turbulence, and horizontal drift of the acoustic pulse due to horizontal winds. This upper limit is typically 2–4 km above ground level (AGL) and 6–8 km AGL for the 404- and 50-MHz systems, respectively. The height coverage of the Erie 404-MHz RASS was from 0.3 km AGL to 3.1 km AGL with approximately 200-m gate spacing, while the 50-MHz data extended from 2.3 km AGL to about 8 km AGL at 450-m gate spacing.

d. Lidar

A 10.6-μm wavelength CO_2 Doppler lidar from NOAA's Environmental Technology Laboratory (ETL)

was operated from a site in the foothills (Betasso) west of Boulder during February 1987. This lidar, described by Post and Cupp (1990), has been used in three earlier studies that focused on downslope windstorms (Neiman et al. 1988; Clark et al. 1994; Ralph et al. 1995). Another Doppler lidar was used in an airborne study of waves in the lee of Mount Shasta (Blumen and Hart 1988). NOAA/ETL's CO_2 lidar receives echoes from solid targets such as dust, snow, cloud droplets, insects, etc., but scattering by 1–3-μm-diameter aerosols is usually dominant. The lidar is sensitive out to a horizontal range of roughly 12–18 km and a vertical range of 2–4 km, except when volcanic aerosols extend the vertical range into the stratosphere or thin high clouds are present. The laser pulse is 300 m long and less than 1 m wide at 10-km range and has no sidelobes, making it an ideal tool for studying air motions (velosity accuracy is 0.6 m s^{-1}) in mountainous terrain. At the time of the observations, reliable backscatter from ''clear air'' was present up to a height of 3 km AGL, although wave clouds at 4 and 10 km were also observed.

e. Satellite imagery

Wave clouds are readily identifiable in geostationary orbiting earth satellite (GOES) visible and infrared (IR) satellite imagery, which is available every half hour at 1-km and 8-km horizontal resolution, respectively. The digitized satellite data allow quantitative analysis of cloud top IR temperatures (provided the cloud fills an IR image pixel) and of horizontal wavelengths using albedo data from the visible images.

In addition to the digital satellite data used for the 8 April 1992 case study, real-time satellite imagery was available at 0.5-h temporal resolution and was examined occasionally over three years for evidence of trapped lee waves. These data were viewed using an experimental real-time data display system, the Denver Advanced Weather Interactive Processing System Risk Reduction and Requirements Evaluation (DARE) workstation, developed and operated at NOAA's Forecast Systems Laboratory (FSL). The relevant information from over a dozen events was either photographed or sketched onto paper from the computer screen before the data aged off. This allowed the wavelengths to be calculated for every image.

3. The waves of 2 February 1987

a. The waves and their environment

On the afternoon of 2 February 1987, between 1700 and 2130 UTC, several cloud bands were parallel to the roughly north–south-oriented crest of the Colorado Rocky Mountains near Boulder, Colorado. Both their orientation relative to the mountains and their approximate two-dimensionality are evident from a photograph of two of these clouds taken looking approximately due west from Boulder (Fig. 2). Visible satellite imagery (not shown) clearly indicates that there were three to six bands oriented north–south. The first three to four cloud bands downstream from the crest were also observed by NOAA/ETL's Doppler lidar, which was sited west of Boulder (Fig. 1) near the center of the cloud photograph. One representative RHI (range–height indicator) from the lidar is shown in Fig. 3.

FIG. 2. Photograph of trapped wave clouds and lenticular cloud looking west from Boulder, Colorado, at 1825 UTC ± 10 min on 2 February 1987. The time of the photograph was estimated by comparing the angle of shadows cast by trees with calculations of the solar azimuth.

The clouds developed on a day when a layer of strong midtropospheric static stability (Fig. 4) was present east of the axis of a midtropospheric ridge (Fig. 5). The operational rawinsonde ascents from Denver (Fig. 4) indicated that the lapse rate increased from 1.1°C km^{-1} between 5.6–6.9 km MSL at 1200 UTC 2 February to 3.4°C km^{-1} between 5.2 and 6.9 km MSL at 0000 UTC 3 February. The stable layer was located below a layer with a lapse rate of 9.8°C km^{-1} and above a layer with lapse rates of 6.9°C km^{-1} and 7.6°C km^{-1} near mountaintop (650–600 mb) at 1200 UTC 2 February and 0000 UTC 3 February, respectively. At both times a moist layer with a dewpoint depression of less than 4°C was present near 6 km MSL. The winds were generally westerly at both times and had very weak vertical shear in the troposphere above the stable layer ($<$2.5 m s^{-1} km^{-1}) at 0000 UTC 3 February (Fig. 4). Because these conditions tend to cause the Scorer parameter [see section 4c(2)] to decrease with altitude across the stable layer, they were favorable for wave trapping to occur in the stable layer. Because the clouds were parallel to and downstream of the mountain crest, and conditions were conducive to wave trapping, it is reasonable to conclude that the clouds marked trapped lee waves.

b. Observations of nonstationarity

Because the lidar receives strong backscatter from clouds, they appear clearly in plots of backscatter in-

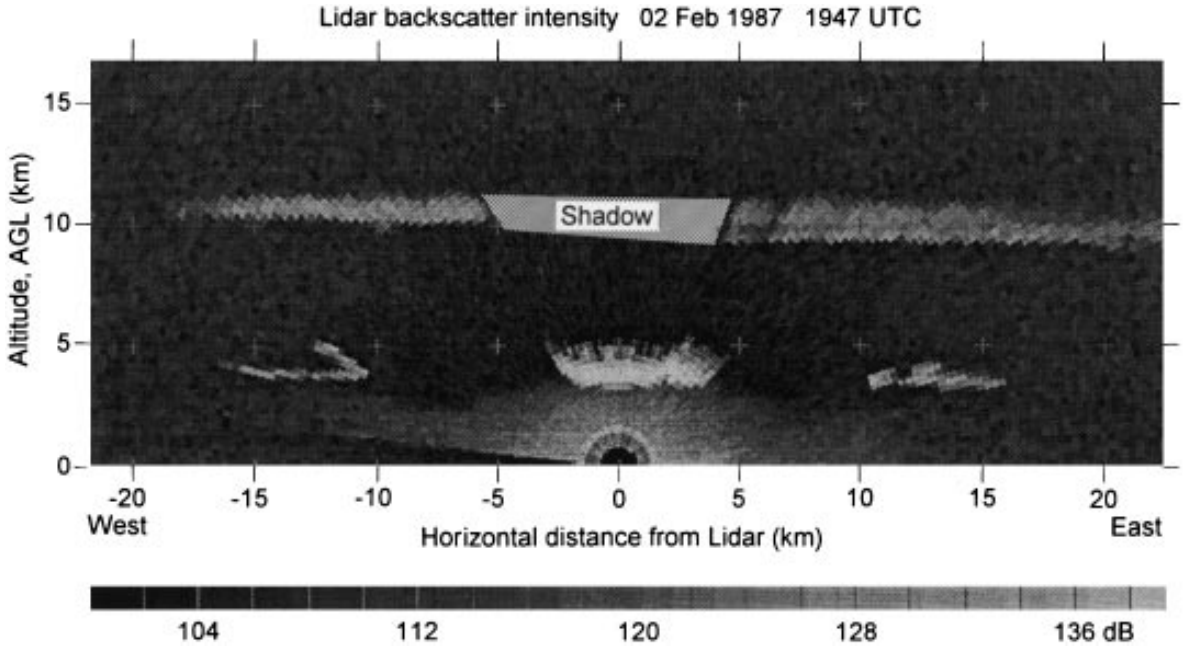

FIG. 3. RHI of lidar-observed backscatter intensity (db) at 1947 UTC 2 February 1987 from Betasso (1.95 km MSL) showing both trapped wave clouds near 3.7 km AGL and a single upper-level lenticular cloud at 10 km AGL.

tensity from RHI scans oriented roughly perpendicular to the wave clouds (Fig. 3). Two types of clouds are evident in this data. At a lower altitude (near 3.7 km AGL) are a series of clouds marking the trapped lee waves, and at a much higher altitude (near 10 km AGL) is a cloud with lenticular structure. Both of these clouds are evident in the photograph (Fig. 2). From the RHI scan, it is possible to measure the upstream and downstream edges of the clouds associated with the trapped lee waves and the altitude of cloud base. From this image, and 14 others like it, the horizontal position of the center of each cloud is measured and plotted as a function of time (Fig. 6). This plot reveals the rather regular increase in horizontal wavelength from 11.2 km

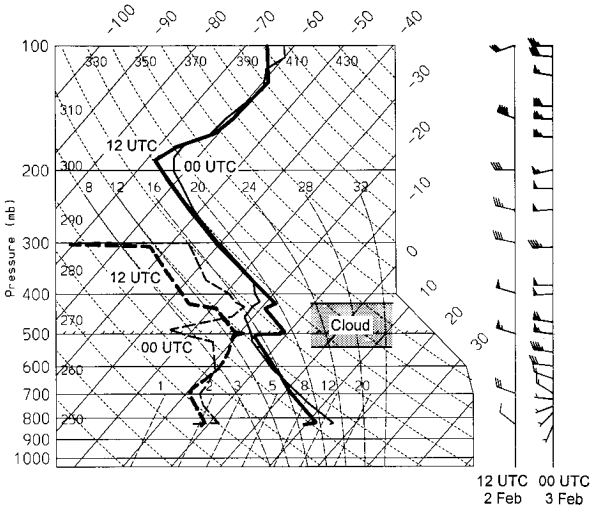

FIG. 4. Skew *T*–log*p* soundings from Denver, Colorado, through the wave environment at 1200 UTC 2 February (bold) and 0000 UTC 3 February (thin) 1987. The vertical range of positions of the trapped lee-wave clouds observed by lidar is also shown. Wind vector flags represent 25 m s^{-1}, full barb 5 m s^{-1}, half barb 2.5 m s^{-1}.

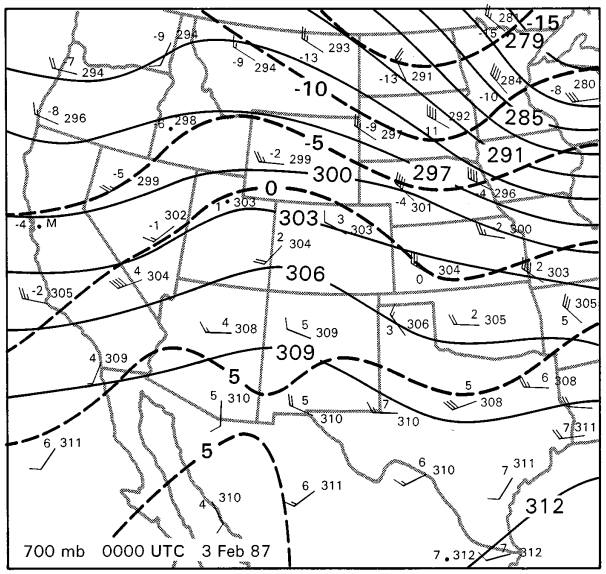

FIG. 5. The 700-mb geopotential height (dam, solid) and temperature (°C, dashed) analysis at 0000 UTC 3 February 1987. Wind flags and barbs are as in Fig. 4. The 700-mb geopotential heights and temperatures rounded to the nearest dekameter and degree are plotted.

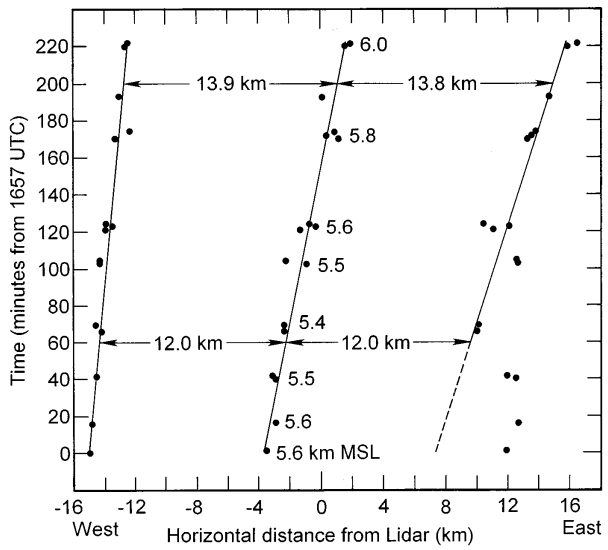

FIG. 6. Time series of wave cloud positions over 3.6 h, based on lidar observations from 2 February 1987. The wavelengths at two times are labeled, as are the altitudes (km MSL) of the trapped wave clouds in each RHI. Solid curves are least squares best fit to the data. Dashed line is an extrapolation of the best fit curve from data after 1800 UTC.

initially to 14.0 km 3.5 h later. This yields a rate of wavelength increase of 0.8 km h^{-1}, or 6% of a wavelength per hour. Although most of the data points line up closely to the least squares best fit lines, a few points marking the third wave cloud (located downstream of the photo in Fig. 2) between 0 and 50 min were 4 km farther downstream than would be expected if the horizontal wavelength were spatially uniform. This difference disappeared in less than 20 min as the third wave cloud moved upstream. Although the exact speed at which this transition occurred is uncertain, it bears some similarity to the behavior reported by Förchtgott (1957) mentioned in the introduction. It could also be related to changing upstream conditions, which could have caused a wavelength change that had just propagated downstream from the mountain crest to the position of the third wave cloud shortly after the observations began. This unusual upstream jump, and the following wavelength increase, are also seen in idealized simulations of nonstationarity by ND96a, in which constant upstream conditions were used. Throughout the lidar measurements, the base of the wave clouds remained nearly constant, varying by only ± 300 m around 5.7 km MSL (Fig. 6), without a clear temporal trend.

Visible satellite images at 1931, 2031, and 2131 UTC (not shown) portray the wave clouds well enough to measure their wavelengths, which are 13.4 km at 1931 UTC (very close to the 13.2-km wavelength measured simultaneously by the lidar), 14.5 km at 2031 UTC, and 16.1 km at 2131 UTC. These data indicate that the rate of wavelength increase became 1.3 km h^{-1}, or 9% h^{-1}, an increase from that measured earlier using lidar data.

c. *The relationship between the wave cloud and wave motions*

In addition to the information about wavelength, the lidar provides unique measurements of the wave-perturbed flow and its relationship to the wave clouds. This is displayed in Fig. 7, where the raw backscatter intensity and radial Doppler velocities are shown, as well as several parameters calculated from the radial velocity data. Horizontal and vertical motions were calculated, assuming that the radial velocities were unaffected by any vertical motions (an assumption that is reasonable only at low elevation angles) and that the flow was two-dimensional and in the plane of the cross section (Mohr et al. 1986). This technique was used recently in a sea-breeze study by Banta et al. (1993). Because the RHI was oriented nearly perpendicular to the waves, the horizontal wind approximates the wave-normal wind. The cloud outline determined from the backscatter intensity is superimposed on each panel of Fig. 7. The domain shown in Fig. 7 is reduced from that of the entire original scan (Fig. 3) because reliable velocity data were only available with useful spatial continuity below 3 km AGL, which is mostly below the clouds, and out to 12-km range. Also, the elevation angle had to be relatively small for the calculations not to be biased too greatly by vertical motions. In order to make the calculations, the original data were transformed from a polar coordinate system to a Cartesian, and velocities were averaged using a Cressman approach with approximately 1.5-km distance of influence along a radial, and two beams in elevation angle. Unlike other observations of trapped waves made earlier, these lidar data provide a nearly instantaneous (60 s) and spatially continuous (although two-dimensional) measurement of the flow, with simultaneous measurement of the cloud location.

Although the data editing reduced the usable domain to roughly 3 km deep and 10–12 km long, which is less than one horizontal wavelength, the kinematic fields clearly contain an undular structure that implies approximately the same horizontal wavelength of 13.5 km that was determined from the cloud positions (Fig. 3). A perturbation horizontal velocity of about 4 m s^{-1}, estimated from an altitude of 2 km between 4- and 10-km horizontal positions in Fig. 7c, and a vertical motion amplitude of greater than 5 m s^{-1} (Fig. 7d) are apparent. The presence of a true rotor, with easterly flow below its axis and westerly flow above its axis, is more clearly documented than in numerous earlier studies that depended on multiple passes of aircraft at a limited number of altitudes. The rotor axis is found 1.5 km below the upstream edge of the eastern trapped wave cloud in Fig. 7. The rotation that appears when the ''rotor cloud'' is viewed over time is based on the strong vertical shear

at and immediately beneath the cloud altitude, not the presence of easterly flow at the lower part of the cloud. These characteristics of the rotor are consistent with earlier observations (Kuettner 1959; Queney et al. 1960), but the very undular nature of the flow suggests that the conditions do not represent hydraulic jump–like behavior (Kuettner 1959) that is now more commonly connected to downslope windstorms (Smith and Sun 1987).

These data also uniquely illustrate the connection between the wave clouds and the kinematic fields associated with the trapped mountain wave, including downward motion found at the downstream edge of the first wave cloud and upward motion at the upstream edge of the second wave cloud. Of particular interest is the observation that the upstream edge of the second wave cloud is downstream of the maximum in upward vertical motion. This relationship is to be expected in a gravity wave for which the vertical displacement of an air parcel is above its original unperturbed altitude, only downstream from the position of maximum upward motion; that is, there is a 90° phase difference between vertical motion and vertical displacement. This implies that if the unperturbed condition is unsaturated, then saturation can only occur where the wave has displaced the air upward from its unperturbed state, which must occur downstream of the position of maximum upward motion. The exact position of the wave cloud downstream from the upward motion maximum is then determined by the amount of subsaturation with respect to water, or with respect to ice if the temperature is below approximately −40°C in the unperturbed flow (Heymsfield and Miloshevich 1995).

4. The waves of 8 April 1992

a. The waves and their environment

On 8 April 1992 several approximately parallel bands of clouds were present over northern Colorado and extended more than 150 km east of the mountains as seen in visible satellite imagery (Fig. 8). A sequence of images shown in Fig. 9 illustrates the evolution of the cloud field, from which an increase in the eastward extent of the wave clouds with time is apparent, as is the northward increase in horizontal wavelength. Numerical simulations described below confirm that these clouds resulted from trapped lee waves.

1) WIND AND STATIC STABILITY

The waves existed in an environment dominated by westerly flow (Figs. 10–12), with the maximum cross-mountain flow of 35–40 m s^{-1} near the tropopause at 13 km (Figs. 11 and 12a). Significant vertical shear was present primarily in the layer from 4 to 6 km, where wind speeds increased from 5 to 20 m s^{-1}. This shear layer was associated with the southern edge of the zonally oriented, midtropospheric, polar front (Fig. 10). A 500-mb short wave thermal ridge over the Colorado Rocky Mountains was situated at the warm boundary of the front, and a jet stream core of about 60 m s^{-1} near 300 mb over the northern Great Plains (not shown) was coupled with the front. A layer of strong static stability from 4 to 6 km was present within the frontal zone above the profilers and was coincident with the zone of strong vertical shear (Figs. 11 and 12). This evidence of the front is similar to that documented by Neiman et al. (1992) using RASS and wind profilers in a study of lower- and midtropospheric fronts. Although the operational 12-h rawinsonde ascents show that a change in this frontal layer occurred during the 12 h after 1200 UTC 8 April (Fig. 11), it was the RASS and wind profiler data that documented the speed and character of the change, most of which occurred between 1800 and 2200 UTC (Fig. 12). Note that the RASS temperatures agree well with the rawinsonde data at the synoptic times (Fig. 11). These data also show that a well-mixed boundary layer had developed east of the mountains to about 4–4.5 km by 2200 UTC 8 April. Above the midtropospheric stable layer, the stability decreased with height up to about 9 km, where there was almost no vertical shear until about 2000 UTC. The vertical distribution of moisture, as determined by the 1200 UTC Grand Junction, Colorado (not shown), and Denver soundings, was ideal for revealing the lee waves, because the stable layer was the only layer that was near saturation. Hence, wave clouds could readily form in the stable layer and would not be obscured by other clouds, at least until later when high clouds did develop (Fig. 11).

2) THE WAVE CLOUDS

On the basis of data from the 8-km resolution GOES satellite IR channel 8 (not shown), the cloud-top temperature was between −11.5°C and −16.5°C, which corresponds to RASS and rawinsonde temperatures at heights of 5–6 km. Because the 8-km resolution satellite IR measurement is an average over areas that are not filled with cloud, it may be expected that this measurement is biased toward warmer temperatures representative of the ground. Hence, the actual cloud tops may be somewhat higher.

The height of cloud base may be determined in a similar way using a ground-based infrared radiometer or a ceilometer (Shaw and Fedor 1992). Although neither of these instruments was available at the profiler site, they were present 50 km to the south at Denver's Stapleton International Airport (Fig. 1). The ceilometer showed intermittent clouds with bases near 5.1 km after 2000 UTC, and the radiometer simultaneously showed intermittent clouds with cloud-base temperatures between −11°C and −15°C, corresponding to heights of about 5 km. In addition, the National Weather Service observer at Stapleton reported scattered clouds with bases at 4.0 and 4.9 km MSL from 1752 to 2150 UTC.

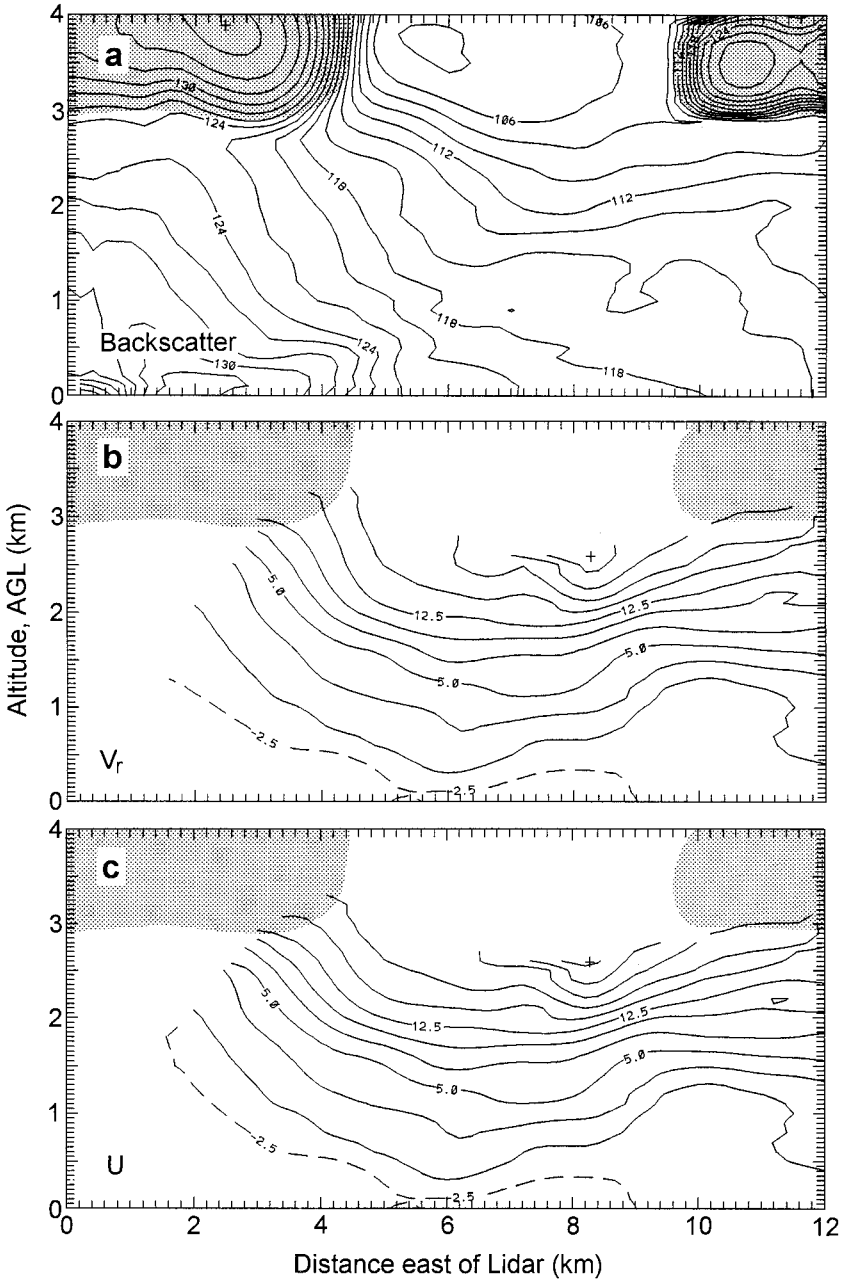

FIG. 7. RHI scans from 1947 UTC 2 February 1987 of lidar-observed (a) backscatter intensity (db), (b) radial velocity (m s^{-1}), (c) horizontal velocity (m s^{-1}), (d) vertical velocity (m s^{-1}), (e) wind vectors in the plane of the RHI, and (f) streamlines. Here, (c), (d), (e), and (f) are determined from integration of the two-dimensional continuity equation assuming zero vertical motion below the lowest scan angle and no flow normal to the plane of the cross section. Shaded regions show approximate positions of the trapped lee wave clouds within the analysis domain, as determined from the lidar-observed backscatter shown in (a).

Because the wave clouds were present over both sites, it is likely that the conditions were approximately the same at the profiler site, a conclusion that is generally supported by the strong similarities between the Denver soundings and the wind profiler and RASS data at 1200 UTC 8 April and 0000 UTC 9 April (Fig. 11). From this analysis, it appears that the wave clouds were located in the layer between roughly 4 and 6 km and were most likely less than 1 km thick, although their exact thickness is poorly defined.

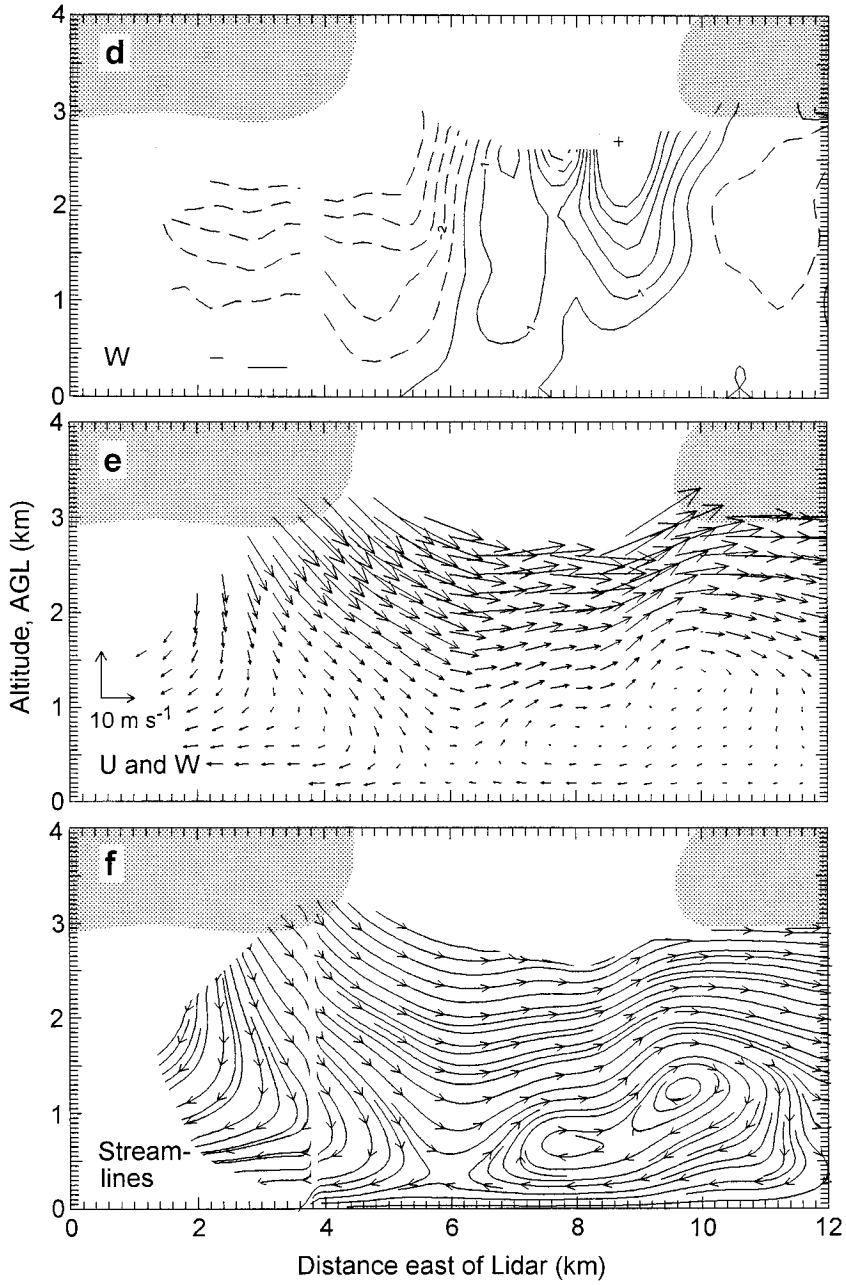

FIG. 7. (*Continued*)

b. Observations of nonstationarity

1) SATELLITE-OBSERVED HORIZONTAL WAVELENGTH

The horizontal wavelength of the trapped lee wave clouds was most accurately determined from the digital visible satellite data and was measured along the four lines in Fig. 13 at the four times shown in Fig. 9. For example, at 2030 UTC, the average wavelength along line *aa′* was 23 km, along line *bb′* it was 17 km, along line *cc′* it was 14 km, and along line *dd′* it was 10 km. Not only did the wavelength vary from longer in the north to shorter in the south, it also varied across the waves, as is apparent along line *bb′* (Fig. 14), where at 2030 UTC it decreased towards the east from 17 km to 14 km. In addition, the wavelength along line *bb′* increased from 16 to 20 km during the interval 1930–2100 UTC, as measured from the first three wave crests downstream from the mountains (Fig. 14). This corresponds to a 14% h^{-1} increase. The cause of this spatial and temporal variability and the connection between them is examined below. The first three wave crests were

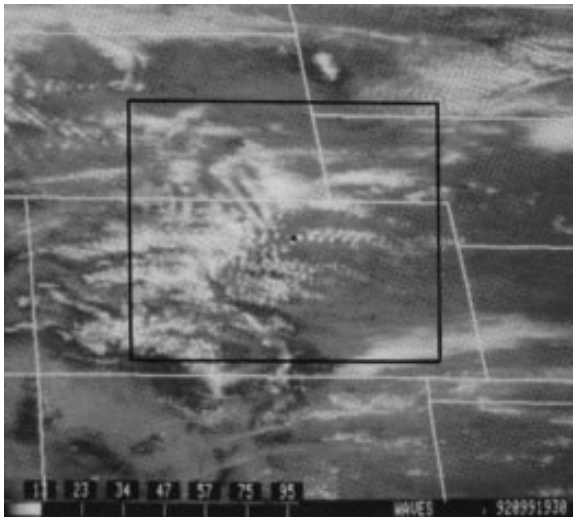

FIG. 8. GOES visible satellite image of mountain wave clouds at 1930 UTC 8 April 1992. State borders (white lines) are drawn with Colorado in the center. The domain shown in Figs. 9 and 13 is shown with bold black lines. The Platteville wind profiler site is marked by a black dot.

chosen because they clearly document the temporal change in wavelength closest to the mountains. The use of many more wavelengths introduces error into the measurement due to interference between wave packets with differing group velocities that were created at different times. This interference has recently been shown in ND96a,b). (After renavigating the satellite images based on terrain features, the longitude and latitude appear to be accurate to within about 1 km and 3–4 km, respectively.)

2) PROFILER-OBSERVED VERTICAL MOTIONS

Direct measurements of vertical air motions were made by both the 50- and 404-MHz radar wind profilers at Platteville on this day, which were at times situated within the train of lee wave clouds (Fig. 9). Only data from the 50-MHz radar are shown here (Fig. 15), because the 50-MHz radar sampled vertical velocities more frequently (see section 2) and the 404-MHz data were very similar. [The similarity of the data also suggests that the 50-MHz data were not contaminated significantly by specular echoes from tilted scattering layers, an issue that has concerned the VHF profiler community (e.g., van Baelen et al. 1991; Larsen and Röttger 1991). This conclusion is also supported by the results of Ralph (1991) and McAfee et al. (1994).] Both in this study and in past work, the temporal variability seen in the time series of profiler-observed vertical motions can be interpreted as a signature of nonstationarity of the lee waves. This sensitivity of profilers to time variations arises because of the large horizontal gradients of vertical motions that are present in trapped lee waves. These large gradients allow even relatively small changes in either the orientation or the horizontal wavelength to change not only the amplitude of the vertical motions observed above a fixed site, but also the sign, as shown in Ralph et al. (1992).

Unlike past studies, in this study profiler records are compared with observations of wave clouds from the visible satellite imagery. Examination of a time sequence of albedo measurements (Fig. 14) along line bb' in Fig. 13, which crosses the profilers, clearly shows the drift of wave crests downstream with time relative to the profiler site. During the 1.5 h shown in Fig. 14, the wavelength drift increased downstream from nearly zero at the top of the easternmost prominent mountain ridge to roughly half a wavelength at the radar site. It should also be noted that the wavelength and relative phase of the waves farther downstream along the wave train continued to shift, although in a somewhat less systematic manner. As should be expected under these conditions, both wind profilers recorded a change in the sign of the vertical velocity over roughly this same time interval. However, there is some indication that the profiler-observed vertical motions are not in the proper phase with respect to the cloud images. This probably occurs because errors in the navigation of the satellite images could easily be as large as ± 3 km, which is significant for a wave with a wavelength of 16 km. Additionally, irreversible processes such as mixing and precipitation should shift the center of a wave cloud from the location of maximum upward vertical displacement. This study indicates that future attempts to correlate trapped wave phases indicated by cloud with profiler-observed vertical motions would require the precision available from ground-based cloud photogrammetry or RHI scans from lidar, as used in section 3.

3) THE VERTICAL STRUCTURE

Although satellite imagery alone cannot define the vertical structure of the waves, the presence of up to 15 consecutive wave clouds downstream of the mountains indicates that significant trapping of wave energy must have occurred, as confirmed by the simulations presented below. Large vertical motions of about 1–2 m s^{-1}, measured by the profilers (Fig. 15), indicate that vertical velocity disturbances extended from the lowest (2 km) to the highest (18 km) radar range gates, well beyond the vertical range of the trapped wave clouds. As has been established by Ralph et al. (1992), such radar data can be used to determine the vertical structure of lee waves. The two primary criteria used to distinguish vertically propagating waves from trapped waves are that in conditions dominated by vertically propagating waves the stratosphere is significantly disturbed and the sign of the wave-induced vertical velocity changes with height. These criteria were sufficient to distinguish the two modes in their study, which involved waves created by relatively narrow mountains roughly 800 m tall. Here, the radar data suggest that above the

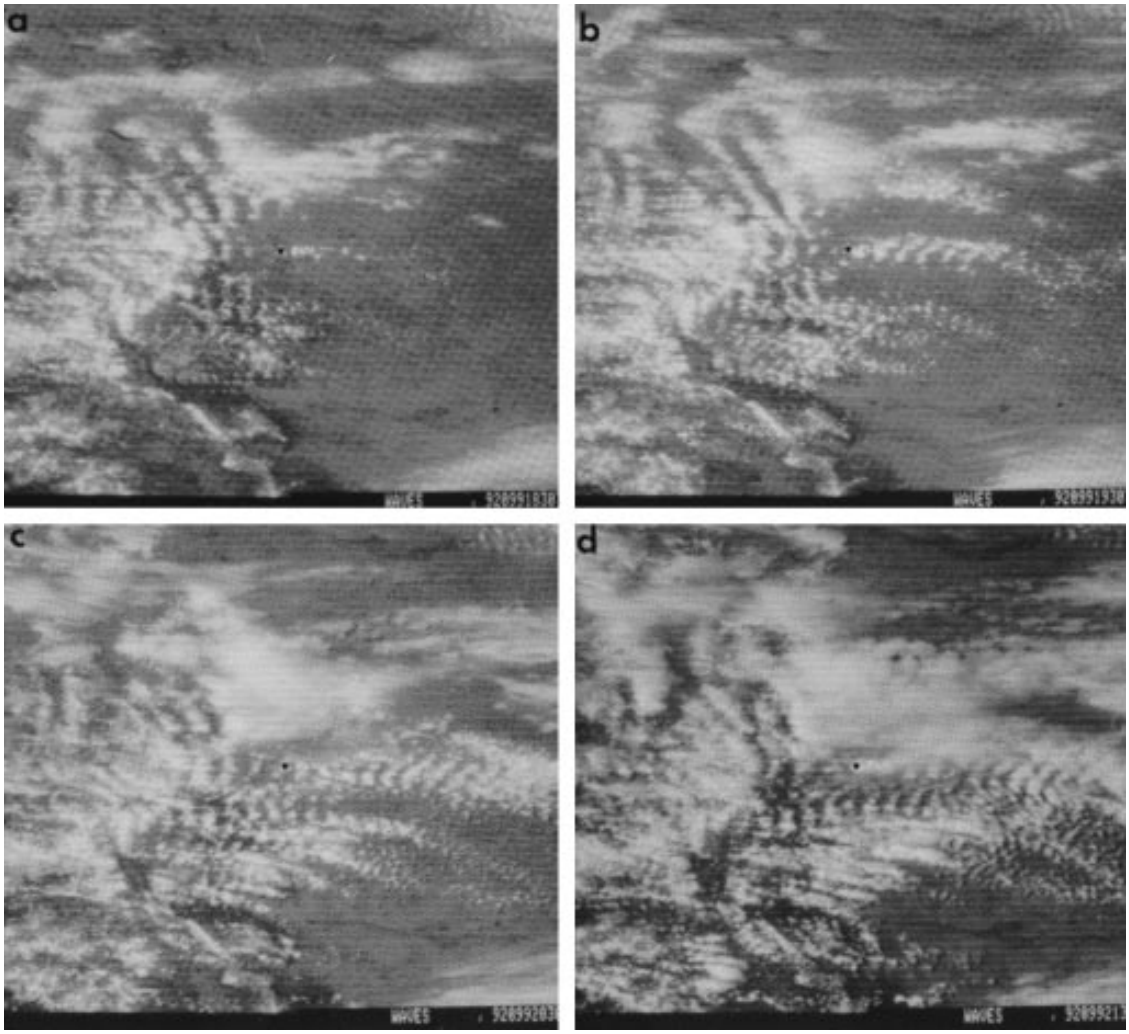

FIG. 9. GOES visible satellite images at (a) 1830, (b) 1930, (c) 2030, and (d) 2130 UTC 8 April 1992. The domain shown is as marked in Fig. 8. A black dot at the center marks the wind profiler site.

well-mixed boundary layer the sign of the vertical motion did not change with height in the troposphere during the interval containing the wave clouds (Fig. 15), but it is evident that substantial wave energy was also present above the tropopause. These observations suggest that both vertically propagating and trapped modes were present, a result that is consistent with the broader and taller mountains present in this case compared with the earlier study. It is also possible that the trapped waves leaked energy into the stratosphere, where the energy propagated away vertically. Such behavior has been noted both in analytical solutions and numerical simulations (Wurtele et al. 1987; Keller 1994).

After the disappearance of the trapped wave clouds over the profilers, there was a noticeable change in the character of the vertical velocity profiles. After about 2200 UTC, the vertical velocity perturbations in the wave cloud layer weakened substantially and there was more of a tendency for the vertical velocity to change sign with height in the troposphere (e.g., see especially between 2200 and 2300 UTC). Thus, 2200–2300 UTC seems to mark a transition away from the dominance of the trapped mode to behavior more representative of vertically propagating waves. This transition is explored below.

c. Evolution of the wave environment and its relation to changing wave structure

This section uses both numerical simulations and linear theory to relate the observed changes in the trapped waves to the observed changes in vertical profiles of static stability and wind shown in Fig. 12. Profiles of wind and temperature from several times during the day, which represented the changing wave environment, were used to initialize a nonlinear numerical model that simulated the mountain waves. Linear theory is used to

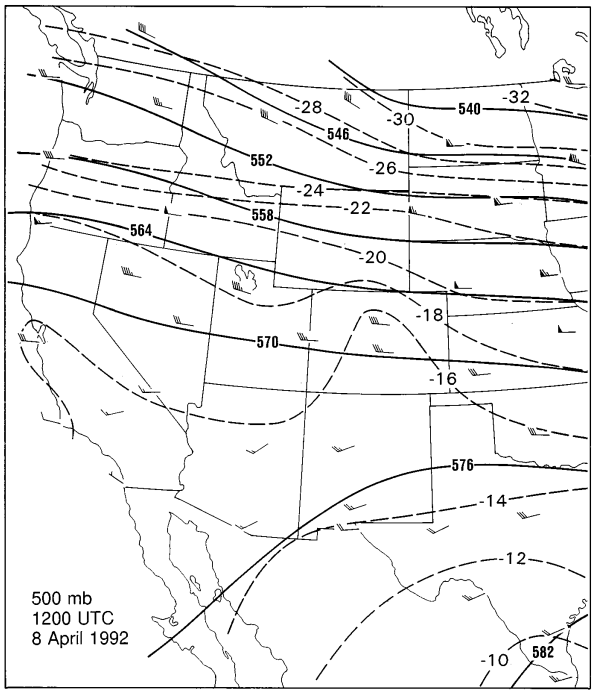

FIG. 10. The 500-mb geopotential height (dam, solid), and temperature (°C, dashed) analysis at 1200 UTC 8 April 1992. Wind flags and barbs are as in Fig. 4.

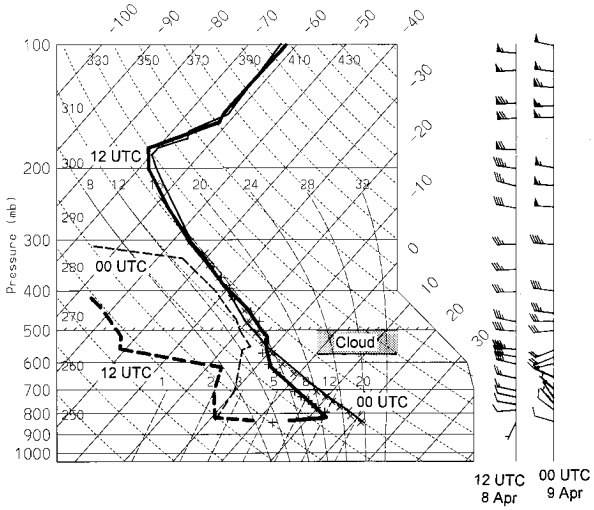

FIG. 11. Skew T–log$p$ soundings from Denver, Colorado, through the wave environment at 1200 UTC 8 April (bold) and 0000 UTC 9 April (thin) 1992. The vertical range of positions of the trapped lee wave clouds observed by satellite and ceilometer is also shown. Wind flags and barbs are as in Fig. 4. One-hour-averaged RASS T_v measurements are shown for 1130 UTC (+) and 2330 UTC (×) 8 April 1992.

examine the relationship between the observed and simulated trapped waves and their environment.

1) SIMULATIONS

Hourly observations from wind profilers up to approximately 16 km MSL and from RASS up to 8 km MSL, combined with 12-h rawinsonde temperature data above 8 km MSL, were used as initial conditions for a nonhydrostatic, nonlinear, two-dimensional numerical model that has been used extensively to simulate mountain-generated gravity waves (Pihos and Wurtele 1981; Sharman et al. 1988). The wind and potential temperature profiles used as initial conditions are shown in Fig. 16. Wind and static stability were assumed constant above 16 km MSL, which is above the tropopause near 13 km. The model used 100 evenly spaced vertical levels 500 m thick, beginning at 1.6 km MSL, with the upper boundary placed high enough (50 km) to avoid reflections from the upper boundary in these relatively short simulations. A horizontal domain of 100 km, with 0.75-km grid spacing, was used with cyclic lateral boundary conditions. The cyclic lateral boundary condition did not affect the results, as the simulations were stopped well before the waves reached the downstream boundary. The lower boundary was horizontal except for a rectangular obstacle 0.5 km tall and 2.25 km wide. The model base was set at 1.6 km MSL to represent conditions east of the mountains where the observations were made. The obstacle was chosen so as to force a broad range of horizontal wavelengths under the assumption that the primary wave response on that day was a resonant mode; that is, the atmospheric structure, rather than dominant horizontal wavenumbers contained in the much larger and more complex mountains in the real case, would determine the wavelength of the trapped lee waves. This assumption proved correct, as illustrated in Fig. 17, which shows vertical motions 66.7 min into each of the five simulations initialized with the conditions shown in Fig. 16. In each run there appeared a well-developed set of waves with maximum amplitude roughly at the observed cloud level (4.5–5.5 km). The vertical orientation of the phase lines is indicative of trapped waves. The 1730 UTC simulation shows the most well-developed and simple wave pattern, with a horizontal wavelength of 12.2 km at the altitude of the cloud layer and maximum vertical velocity amplitude of ± 1.8 m s^{-1}. The horizontal wavelengths, maximum vertical velocity amplitudes, and the altitude of the maximum vertical velocity from the five simulations are given in Table 2. The simulated horizontal wavelengths of 11.3–15.3 km compare with wavelengths of 14–20 km determined from visible satellite images in the vicinity of the profilers, which increased in wavelength from 16.5 to 20.0 km between 1930 and 2100 UTC. The total number of waves in each simulation (3–4 in Fig. 17) is less than the observed (10–11) because the downstream domain was too short, considering the cyclic lateral boundary conditions, to let the simulations proceed much farther than what is shown in Fig. 17. The simulations clearly demonstrate that trapped lee

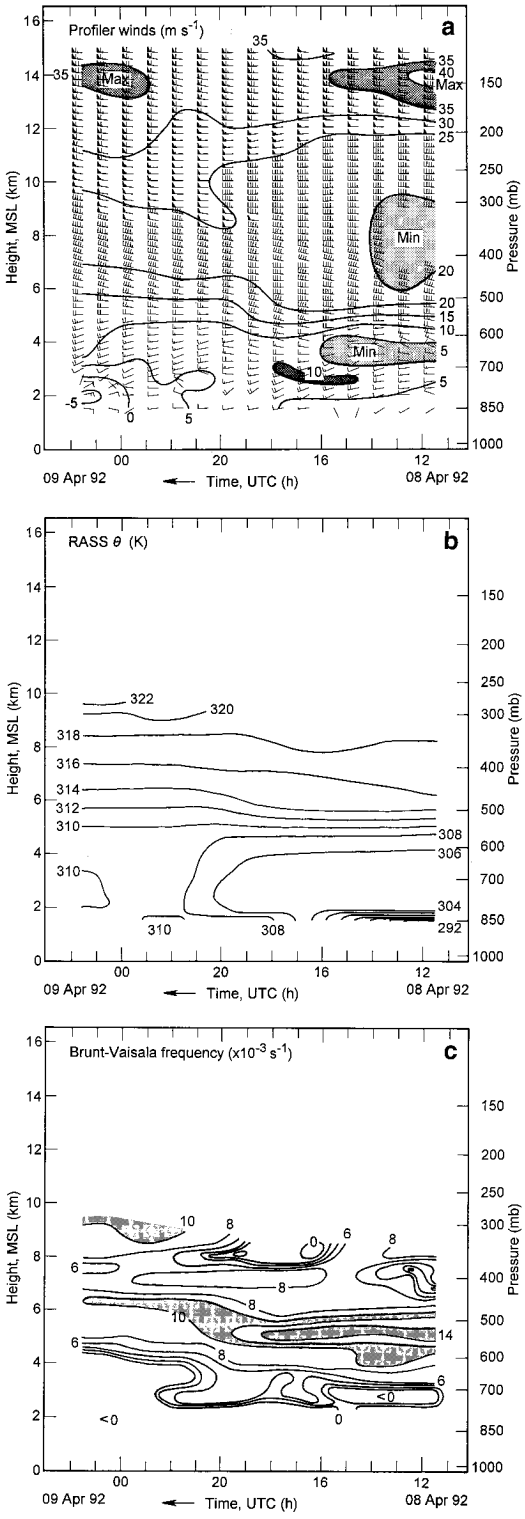

FIG. 12. (a) Time–height section of 1-h averaged horizontal winds (flags and barbs are as in Fig. 4) from the 404-MHz wind profiler and collocated surface data. The cross-mountain wind speed (i.e., the zonal wind component) is shown with solid contours every 5 m s^{-1}. (b) Time–height section of a synthesis of virtual potential temperature (K) observed by the Erie 404-MHz and the Platteville 50-MHz RASS systems corrected for vertical air motion and surface data. (c) Brünt–Väisälä frequency (s^{-1}), determined from (b).

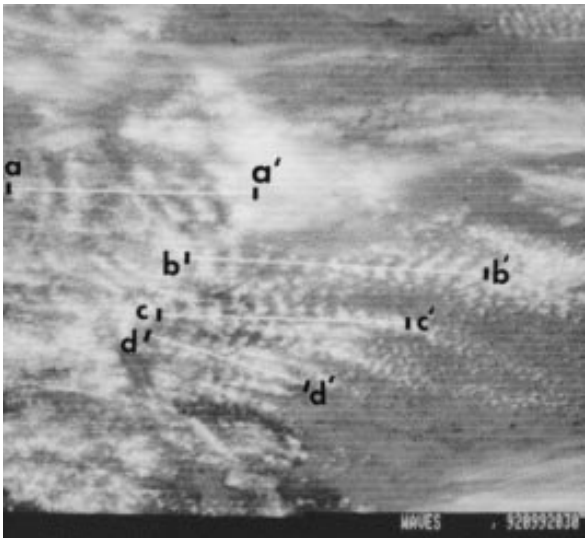

FIG. 13. GOES visible satellite image at 2000 UTC 8 April 1992. The domain shown is marked in Fig. 8. Lines *aa′*, *bb′*, *cc′*, and *dd′* were used to measure wavelength (see text and Fig. 14).

waves could develop under the observed conditions and that an overall temporal increase in wavelength could be attributed to changing background atmospheric conditions. However, the simulated wavelengths are some-

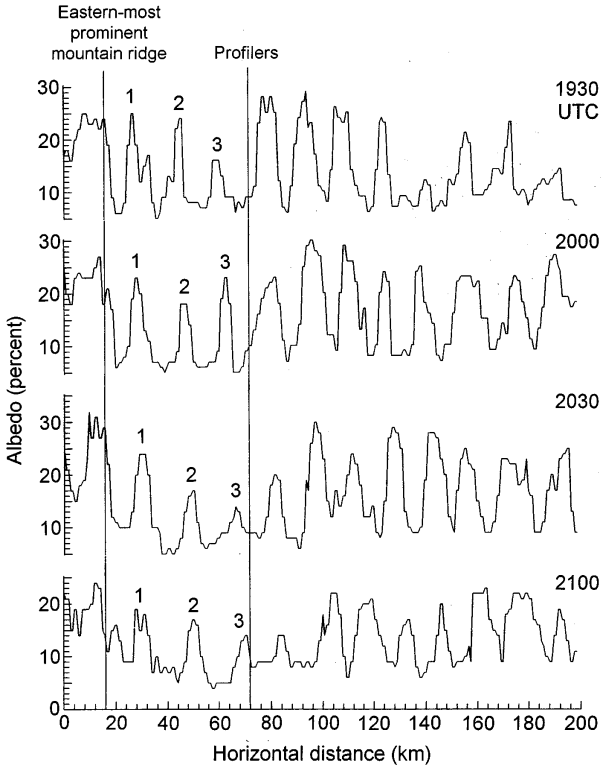

FIG. 14. Sequence of four satellite-observed albedo measurements along line *bb′* in Fig. 13. The first three wave clouds downstream from the Rocky Mountain Front Range are labeled.

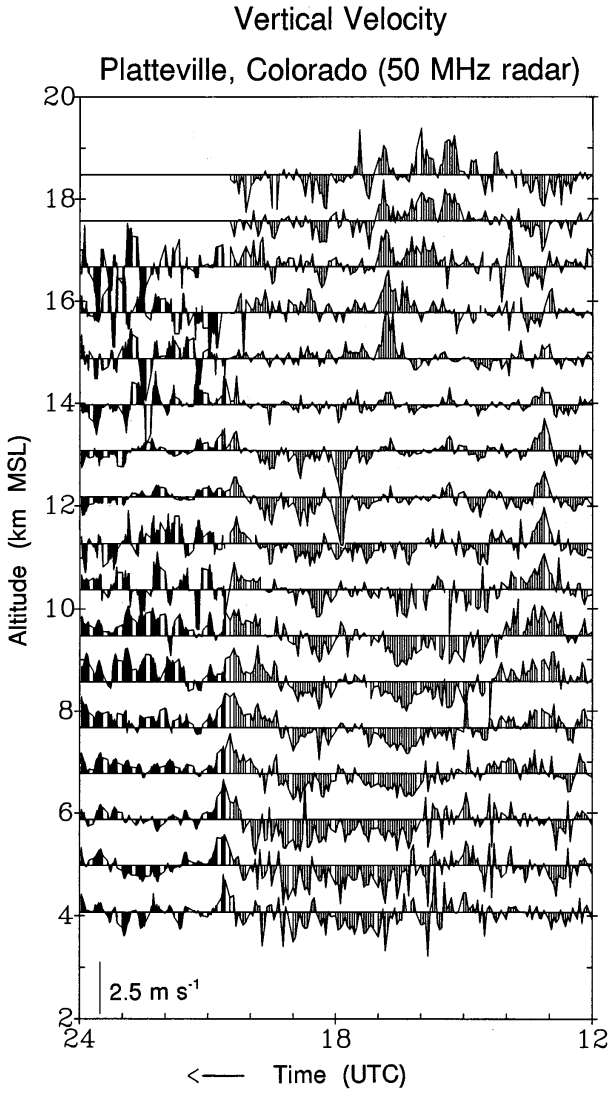

FIG. 15. Vertically stacked vertical velocity time series from the Platteville 50-MHz wind profiler between 1200 UTC 8 April and 0000 UTC 9 April 1992. Note that the sampling characteristics changed at 2041 UTC 8 April.

what shorter than those observed, and the simulated increase in wavelength is interrupted at 1930 UTC (Table 2). The remarkable similarity between the predicted vertical velocity amplitudes of ± 2 m s^{-1} and the observed vertical velocity amplitude of ± 2 m s^{-1}, as well as the fact that they extend with significant amplitude throughout the troposphere, also attests to the accuracy of the simulations and to the fact that the waves represent resonant modes. This agreement is highlighted in Fig. 18, which compares simulated and observed vertical velocity profiles. Similarly good agreement has been found recently in several cases of vertically propagating waves by Prichard et al. (1995), but only in terms of the vertical wavelength. A reduction in the amplitude of the trapped waves in the later simulations is consistent with the conclusion from profiler-observed vertical motions and satellite imagery that the vertically propagating waves became dominant by 2130 UTC. It should be noted, however, that the simulated amplitude of the trapped mode is determined both by the strength of the forcing at the resonant wavelength, which is affected by the height and shape of the mountain, and by the resonance characteristics of the fluid. Figure 18 also shows that the model did not reproduce the significant perturbations observed in the lower stratosphere (see also Figs. 15 and 17). This difference likely arises from the fact that the model used a small, narrow obstacle (chosen to study trapped lee waves) unable to produce the strong vertically propagating waves that the tall, broad mountains in the real case likely excited [see section 4b(3)].

Theoretical studies (Corby and Wallington 1956) indicate that the resonant horizontal wavelength decreases as the thickness of the stable layer increases and is quite sensitive to the thickness of the stable layer. This sensitivity might explain the shortness of the predicted wavelengths relative to the observed, because the vertical resolution of the VHF RASS data (450 m) and the model (500 m) could have inadvertently thickened the stable layer. Additionally, some of the difference could be attributed to the fact that the observations were made downstream of the mountains and should therefore represent conditions in the wave-forcing region approximately 1–2 h earlier under conditions when the wavelength was observed to increase with time. Because both these factors would cause each simulation to underpredict the resonant wavelength for the time representing the initial conditions, they are consistent with the fact that all simulated wavelengths are shorter than observed. Although the fact that the initial conditions were derived from observations made within the waves suggests that significant uncertainties may arise from the inability to separate the perturbations from the background flow, the model is used in the appendix to show that this introduces very small errors in this case, that is, ± 0.3 km uncertainty in the predicted 12.2-km wavelength in the 1730 UTC simulation.

2) COMPARISON WITH LINEAR THEORY

Because the mountains in this case are nearly two-dimensional, the waves are not of great amplitude, and trapped lee waves are often treated well using linear theory (e.g., Foldvik 1962; Vergeiner and Lilly 1970; Wurtele et al. 1996), two-dimensional linear theory should be applicable. For this purpose the square of the Scorer parameter l (e.g., Scorer 1949; Smith 1979),

$$l^2 = \left(\frac{N}{U}\right)^2 - \left(\frac{1}{U}\right)\frac{d^2U}{dz^2} \qquad (1)$$

(where z is altitude, U is cross-mountain wind speed, and N is static stability), is calculated from the 1-h-

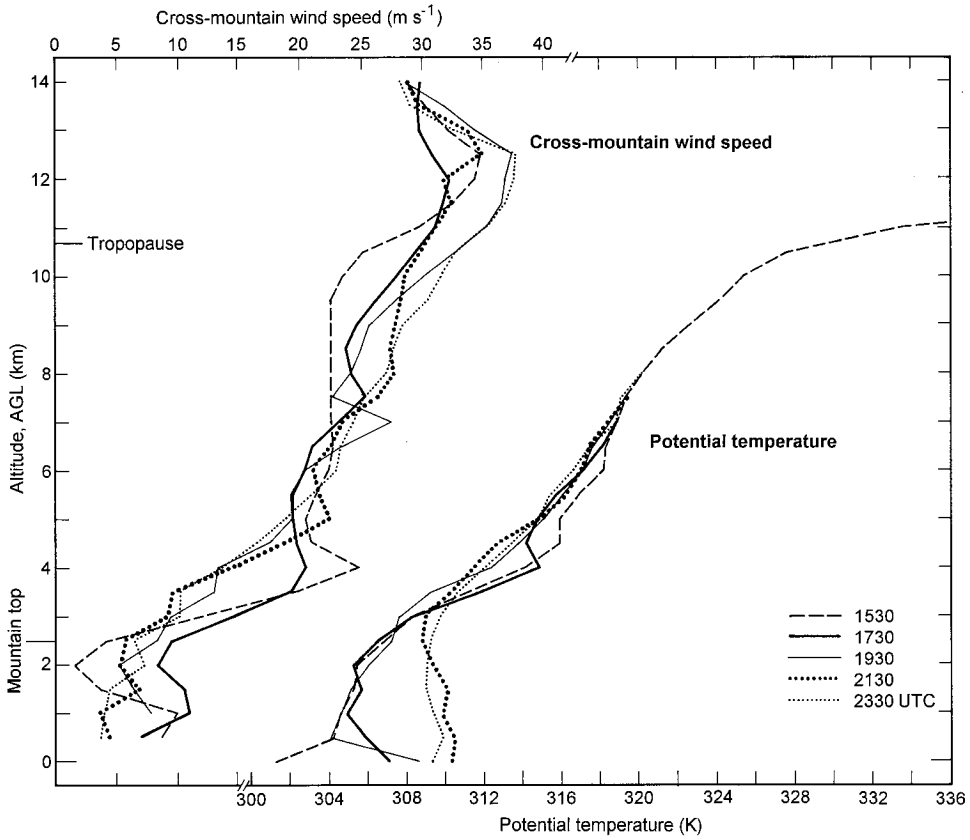

FIG. 16. Initial conditions used in the simulations. Static stability and wind are constant above this domain, which extends 50 km vertically. Winds are from a 404-MHz wind profiler. Potential temperatures below 8 km MSL are from a 50-MHz RASS and above 8 km are from a rawinsonde.

average profiles of T_v from RASS and wind from the wind profilers. This was done hourly between 1200 UTC 8 April and 0200 UTC 9 April. Results at four times are shown in Fig. 19. To quantify the influence of changing static stability and wind profiles on the waves, we show each of the two terms in Eq. (1) in addition to the total Scorer parameter. It should be noted that the winds used to calculate the curvature term, that is, the second term in Eq. (1), were smoothed vertically using five passes of a Hann filter to eliminate vertical scales of less than 1 km that had strongly affected the estimate of the second derivative. Although these calculations should ideally use conditions observed upstream of the mountains, such data are not available for this study. In addition, the 1-h averaging helps to reduce the impact of the wave perturbations, yet possibly retains some of the interesting temporal evolution. An assessment of the uncertainties associated with using the data from within the wave pattern to represent conditions upstream of the mountains in this case is presented in the appendix, where it is shown that the uncertainty is small relative to the simulated and observed changes in the wavelength of the trapped waves.

At 1730 UTC, which is roughly when the wave clouds first became prominent downstream of the mountains, there existed a pronounced stable layer at about the same height as the wave clouds above mountain-top level (Figs. 12b and 12c). This high stability, combined with negative values of the curvature term, created large values of l^2 in that layer (Fig. 19a). A well-mixed convective boundary layer developed up to 4.6 km by midday (Fig. 16) and combined with large positive values of the curvature term to reduce l^2 below the cloud layer. These characteristics, as well as the data above the cloud layer, suggest that the cloud layer was also a layer of maximum l^2. Because gravity waves that had a wavelength short enough to be evanescent in the upper and lower layers may still have been able to propagate within the intermediate layer, this condition strongly favored the trapping of wave energy within the intermediate layer. This result agrees well with the inferences based on the length of the train of lee waves. Although the profilers each measured substantial vertical velocities in the cloud layer, these motions were also linked to similar motions at higher altitudes (Fig. 15). This suggests that significant wave energy had leaked upward from the duct into the decay region, as is also seen clearly in the simulations (Fig. 17).

As can be seen from Fig. 19, the peak of l^2 found in the first profile is still present at 1930 UTC but is less

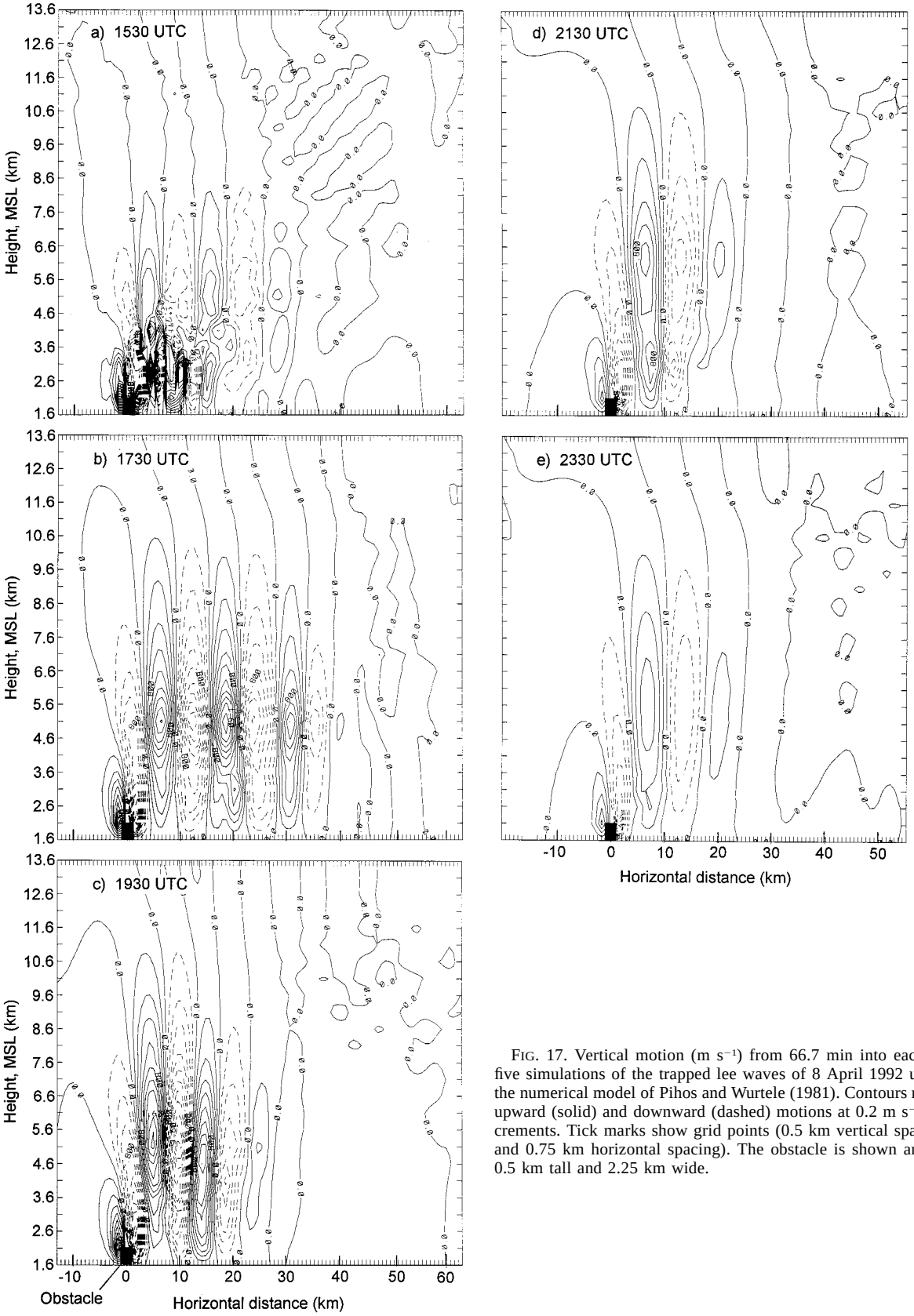

FIG. 17. Vertical motion (m s^{-1}) from 66.7 min into each of five simulations of the trapped lee waves of 8 April 1992 using the numerical model of Pihos and Wurtele (1981). Contours mark upward (solid) and downward (dashed) motions at 0.2 m s^{-1} increments. Tick marks show grid points (0.5 km vertical spacing and 0.75 km horizontal spacing). The obstacle is shown and is 0.5 km tall and 2.25 km wide.

TABLE 2. Simulation results for the 8 April 1992 case.

Time of initial conditions (UTC)	Horizontal wavelength (km)	Maximum vertical velocity in waves (m s^{-1})	Altitude of maximum vertical velocity (km MSL)
1530	11.3	0.3	5.1
1730	12.2	1.8	5.1
1930	9.6	1.8	5.1
2130	15.3	1.1	6.1
2330	15.0	0.7	5.6

prominent by 2130 UTC and is nearly gone by 2330 UTC. This transition, which is most evident between 2100 and 2200 UTC, corresponds to the disappearance of trapped lee wave clouds and the appearance of a broad cloud sheet more indicative of vertically propagating mountain waves (Durran 1986) above the radars (Fig. 9) and to the appearance of a new regime in the observed vertical motions (Fig. 15) dominated by conditions more characteristic of vertically propagating waves (i.e., the sign of the vertical motion changes with height). Although the simulations show that conditions at 2330 UTC were still conducive to the development of trapped lee waves, their amplitude is significantly less than at earlier times (i.e., 0.7 vs 2.0 m s^{-1}). This transition in the l^2 profile appears to be most strongly influenced by the shear layer, initially between 4 and 6 km, that rose to 4.5–7 km and weakened (Fig. 12a). This is captured in the curvature term in the wave cloud layer (Fig. 19),

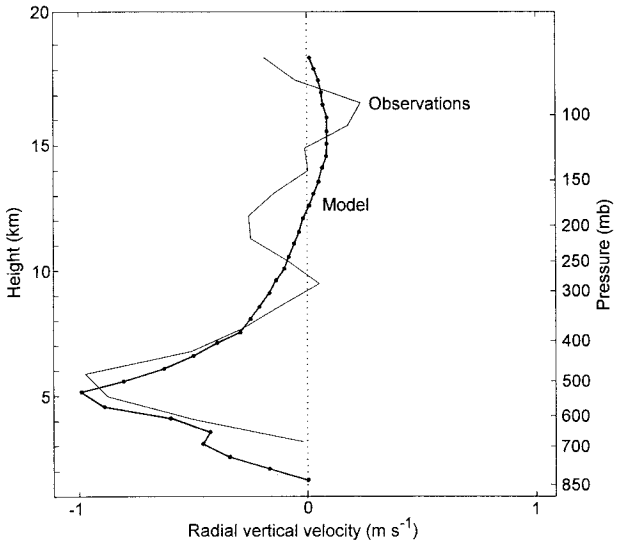

FIG. 18. Comparison between the simulated and observed vertical velocity profiles. Model conditions are from 1910 UTC, 100 min into the run initialized at 1730 UTC (see Fig. A1). Observations are a 30-min average centered on 1910 UTC from the Platteville 50-MHz radar wind profiler. Platteville is 50 km east of the three major Front Range peaks to its west, which are Blue Mountain (47 km west, 2406 m MSL), Fairview Peak (53 km west, 2609 m MSL), and Bear Peak (49 km west, 2578 m MSL). The model profile is from 50 km east of the obstacle's center.

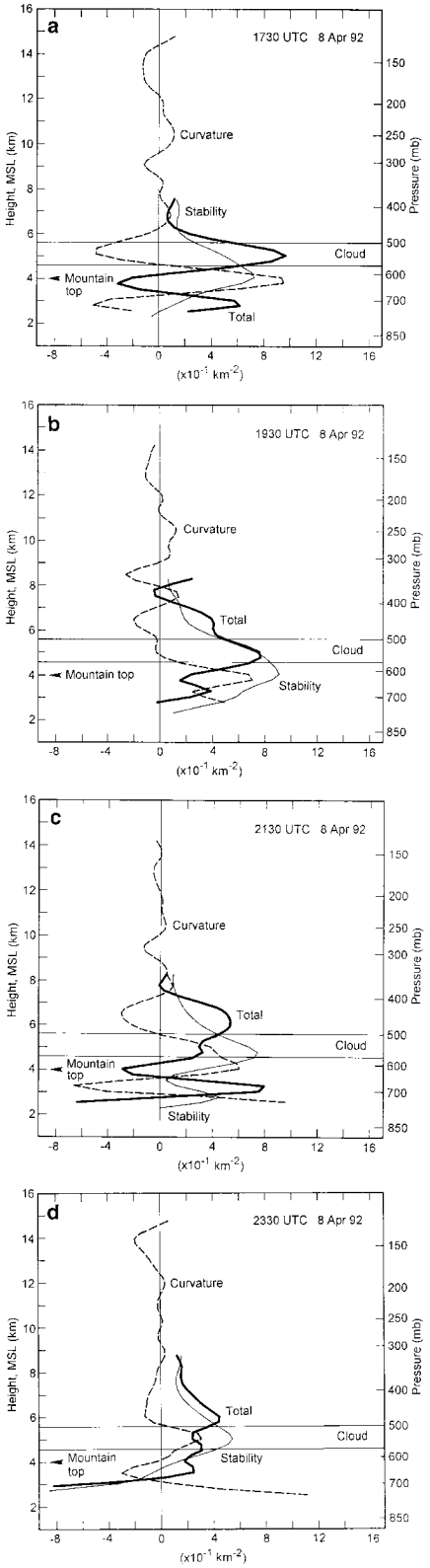

FIG. 19. Vertical profiles of the square of the Scorer parameter l (total, bold) and its two primary terms, i.e., the static stability (thin, solid) and the curvature (dashed) terms at (a) 1730, (b) 1930, (c) 2130, and (d) 2330 UTC 8 April 1992.

which changes from strongly negative to strongly positive between 1730 and 2330 UTC. Although the static stability in this layer decreases substantially at the time of the transition (Figs. 12b and 12c), decreasing winds (Fig. 12a) compensate for this and keep the first term in (1) nearly constant. Hence, it is concluded that in this event the observed transition in dominant wave type was influenced by changes in the curvature term. This is consistent with the conclusion by Crook (1988) that curvature was important in trapping waves generated by gravity currents.

3) ORIGINS OF CHANGES IN THE WAVE ENVIRONMENT

From examination of upper-level charts, such as the one shown in Fig. 10, it is apparent that baroclinic disturbances were passing over the region being studied during the general time of interest. Although there is only a hint of a short-wave baroclinic ridge in the geopotential height field approaching from the west at 1200 UTC 8 April in Fig. 10, there is clearly a thermal ridge. Also, examination of vorticity at that level (not shown) reveals a short-wave ridge in geopotential height upstream of the profilers and a short-wave trough to its west. From the wind profiler data (Fig. 12a), it appears that below 500 mb the ridge axis passed between 2200 and 2400 UTC. Recall the evidence from RASS (Figs. 12b and 12c) of changes in the static stability at the same time. These features appear to be linked to changes in the wave structure, as seen in the satellite imagery and as indicated by the profiler data and Scorer parameter analysis. Under these conditions, one might expect that the approaching baroclinic ridge and implied subsidence helped create a favorable environment for the development of the trapped waves by enhancing the stable layer near mountain top. Similarly, lifting due to the approaching trough after 2200 UTC may have been associated with the observed reduction in the strength of the stable layer. However, as noted earlier, linear theory suggests that changes in the vertical wind shear (curvature) also affected the change in wavelength and wave type. It is likely that those changes as well were closely related to the passage of the ridge axis.

In addition to changes due to baroclinic systems, diurnal effects may have influenced the wave evolution. Deepening of the well-mixed boundary layer downstream of the mountains up to roughly 4.5 km by 0000 UTC 9 April, as seen in the Denver sounding (Fig. 11) as well as in the RASS data (Fig. 12), may have aided the erosion of the lower part of the elevated stable layer containing the waves. This erosion of the stable layer from below is seen in Fig. 16, where the destabilization occurs first at lower altitudes and then works its way upward into the base of the strong stable layer, before the observed transition around 2200 UTC to conditions dominated by vertically propagating modes. As a result, the base of the stable layer rises from 2 to 3 km AGL and thins with time (Fig. 20). Changes in the boundary layer upstream of the mountains and in the mountains themselves (based on time variations of trajectories upstream) are also likely to have modified the waves, although this cannot be studied here. Also, diurnal effects could vary with distance downstream and, thus, so too could the waveguide characteristics. Earlier studies by Holmboe and Klieforth (1957), Queney et al. (1960), and Gerbier and Berenger (1961) also suggested that diurnal changes in the wave environment resulted in an increase in horizontal wavelength during the afternoon, although few data were presented in support of this hypothesis. Further support for the sign of this trend can be found in the conclusions of Corby and Wallington (1956), where it was shown that the wavelength of the first resonant mode was inversely related to the thickness of the stable layer that formed the core of the waveguide and that the wavelength was very sensitive to small changes in the stable layer's thickness under some regimes. The inverse relationship between stable layer thickness and trapped wavelength is observed in this case (Fig. 20, Table 2). In addition, Palm and Foldvik (1960) and Foldvik (1962) used linear theory and idealized exponential vertical profiles of the Scorer parameter to show how horizontal wavelengths would vary, depending on the near-surface value of the Scorer parameter (l_0) and on the rate at which it decreased with height (c). For example, a decrease in l_0 from 4.24 to 3.05 km^{-1}, keeping c constant at 0.225 km^{-1}, would cause a doubling of the trapped wavelength from 10 to

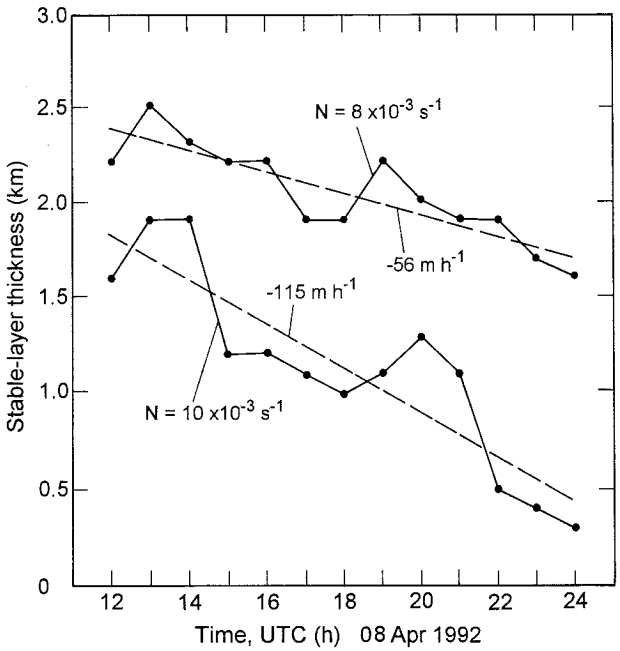

FIG. 20. Temporal evolution of the thickness of the statically stable layer near mountain top in the 9 April 1992 event derived from hourly RASS T_v profiles (Fig. 12). Two thresholds of Brünt–Väisälä frequency N are used. The least squares best fit curves are shown (dashed) and their slopes labeled.

20 km. Such a change in l_0 could easily occur rapidly because it requires only a factor of 2.56 change in U^2 or N^2. Similarly, a reduction of c from 0.275 to 0.115 km^{-1}, keeping l_0 constant at 3.46 km^{-1}, would double the trapped wavelength from 10 to 20 km. However, because a decrease in l_0 would cause a decrease in c, as would be expected if changes were due to changing boundary layer characteristics, the two factors would compensate for one another to some degree.

It is most likely that these three phenomena, that is, the passing baroclinic disturbance, changes in l_0 due to changes in the boundary layer, and the upward erosion of the primary stable layer near mountain top by the deepening convective boundary layer, combined to modify the wave environment. These modifications led first to changes in the trapped wavelength and then to the apparent change in dominant wave mode from trapped to vertically propagating in this case.

5. Summary of observed trapped lee-wave nonstationarity and the average rate of wavelength change

In addition to the two cases presented above in sections 3 and 4 that provide striking evidence of trapped lee-wave nonstationarity, several earlier studies noted in the introduction have documented similar behavior in detailed case studies, although only as a small part of their respective overall studies. This section both summarizes these earlier cases and introduces more than a dozen additional events revealed from sequential visible satellite imagery at half-hourly intervals. All of the events are included in Table 3, where some statistics based on the 24 events are also presented. Although Holmboe and Klieforth (1957) reported anecdotal evidence that the wavelength defined by wave clouds could increase by as much as 30% in 12 h in the lee of the Sierra Nevada, it is not included in Table 3 because the observations on which this conclusion was based were not shown.

a. Cases documented from earlier studies

1) COLLIS ET AL. (1968)

Unique lidar studies of mountain wave clouds were performed in the 1960s east of California's Sierra Nevada using ruby lasers (Collis et al. 1968; Viezee et al. 1973). Because Doppler capability was not available in those studies, they were limited to observing the structure of the wave clouds. However, in one case lidar RHI observations of backscatter from two lenticular clouds at two times 1.3 h apart revealed spatial undulations of the cloud at 11 km MSL (which is unusually high for trapped lee waves) near noon local time on 1 March 1967, a day with conditions favorable for trapped waves to develop (Collis et al. 1968). The wavelength increased from 17.5 to 21.0 km during this time.

2) VERGEINER AND LILLY (1970)

Data from a sequence of two traverses of radar-tracked constant-volume balloons over the Colorado Rocky Mountains on 28 January 1967 over 1.4 h revealed an increase in the trapped wavelength from 11 to 12 km during the afternoon.

Two traverses of constant-volume balloons on 30 January 1967 over 1.5 h revealed a temporal decrease in wavelength from 14.0 to 13.5 km near sunset.

Two traverses by constant-volume balloons on 31 January 1967 over 1.3 h revealed a temporal increase in wavelength from 13.7 to 16.7 km near sunset.

Aircraft traverses across the crest of Colorado's Rocky Mountains were performed on 1 March 1967 at nearly the same altitude over a 2.0-h period. These data revealed an increase in the trapped wavelength from 14.5 to 17.5 km.

3) STARR AND BROWNING (1972)

A high-powered 10-cm-wavelength radar was used to observe undulations of the top of the convective boundary layer in the lee of the United Kingdom's Welsh Mountains on several days. In a sequence of several RHI scans through trapped lee waves on 3 February 1970, they illustrate ''a complex and unsteady wave pattern with a spread of wavelengths between 15 and 30 km.'' Although this event is more complex than the other cases, their data are still amenable to a rough linear fit between 1300 and 1520 UTC, which is two-thirds of the total observed event. Based on this approach, it appears that the wavelength increased from approximately 23 to 29 km during this time, which is early afternoon.

4) WEISS (1976)

A pair of GOES visible satellite images at 1330 and 2035 UTC 27 April 1976 showed up to 22 parallel cloud bands downstream from the Appalachian Mountains. Weiss (1976) presented evidence that the clouds represented trapped lee waves in northwesterly flow. Comparison of the two images shows that the horizontal wavelength increased from 6.6 to 10 km between these times at a rate of 0.5 km h^{-1}, or 6% h^{-1}. It was also shown using rawinsonde ascents 12 h apart that the static stability of the stable layer on which the trapped lee waves formed decreased and the wind speed below the stable layer increased. Although the conclusions were not tested quantitatively, it was suggested that these changes in the wave environment were consistent with a temporal increase in trapped wavelength and that the changes in the environment resulted from a combination of diurnal surface heating and cold advection aloft.

5) MITCHELL ET AL. (1990)

Based on a single high-resolution visible satellite image from 2024 UTC 16 October 1985 that showed an

abrupt change in the horizontal wavelength downstream of Macquarie Island (52.6°S, 158.9°E), it was concluded that the wavelength of trapped lee waves forced by the island had changed between two times at which soundings had been launched from the island. These soundings were then used to show that the wavelength of the resonant mode had decreased from 15.4 to 10.0 km between those times. Based on estimates of the wave's group velocity (10 m s^{-1}) and the fact that the transition occurred over less than two wavelengths (25.4 km), it was possible to conclude that the wavelength change had occurred over less than 1 h, sometime between 1730 and 1830 UTC (0324–0424 local time). This event represents the best evidence of a decrease in wavelength with time, rather than the increase characteristic of most of the other cases. Because the first image is from 0624 local time, which is just after sunrise, and the wavelength change occurred 2–3 h before that, the wavelength change must have occurred during the night.

b. Events documented using real-time visible satellite imagery

Based on the confidence gained from the detailed case study of 8 April, it was decided to document several additional events using satellite imagery alone. As was described in section 2, visible satellite images were viewed as temporal loops using the DARE workstation at NOAA/FSL as they occurred in real time. Events were selected on random days over roughly three years when it was possible to view and record the data. Only those cases in which a wavelength change was apparent were recorded. Although this precludes the possibility of any firm conclusions about the frequency of such events, it does provide a sample from which the magnitude of the wavelength change that occurs in the atmosphere can be ascertained. Only events in which at least two distinct wave clouds were present were selected. These clouds had to be nearly parallel to one another and nearly parallel to and downstream of mountain ranges. The area included all of Wyoming and Colorado, and the parts of Utah, New Mexico, and Arizona that are close to Colorado. One event from Oregon is also included. Cloud positions were recorded usually at 30–60 min intervals for up to several hours. Because the wavelength was of interest rather than the exact location of the waves, it was unnecessary to renavigate the images to their proper geographic location. However, because the results are interpreted as changes at a specific location, an attempt was made to measure the wavelength along the same line relative to the ground, and errors in this attempt create some uncertainty in the numerical values calculated. For several of the events, this method was used along more than one line, and the results were averaged to reduce this uncertainty and to better represent changes through most of the trapped wave field. On three of the days, the wavelength changes varied enough over the domain and time that two separate measurements are included as independent cases and are labeled as such. Results from the 15 cases measured from satellite images using this method are included in Table 3.

c. The average rate of change of wavelength of trapped lee waves exhibiting nonstationarity

Table 3 presents statistics from 24 events where nonstationarity was measured. The average of all these events, excluding the one extreme case from Mitchell et al. (1990), is an increase in wavelength of 9.2% h^{-1} or 1.5 km h^{-1}. It appears that the wavelength can often increase by 10% h^{-1}, and events with changes of up to 28% in 1 h were noted. Although these data do not represent a systematic study of how frequently wavelength changes occur, of the 24 events measured, the wavelength was observed to increase in 20. Most events were observed during daylight hours when diurnal heating was present, except for the most dramatic case of a decrease in wavelength with time and one of the two cases of a small decrease with time. These data, along with the conclusion from the detailed case study of 8 April 1992 presented in section 4 that a deepening convective boundary layer played a role in that event, suggest that diurnal heating may be the dominant mechanism leading to temporal changes in wavelength during the day in many cases. The preference for daytime wavelength increases is difficult to explain in terms of the passage of synoptic-scale weather systems and, thus, reduces the likelihood that the temporal wavelength changes are mostly a response to their passage. However, there are events in which the synoptic changes dominate, as probably occurred in the Macquarie Island event. It is also likely that such island locations are less affected by diurnal cycles because of the maritime nature of the upstream environment. It is unclear how this apparent preference toward wavelength increases is related to the nonstationary behavior documented by ND96b in idealized simulations for which upstream conditions were steady.

6. Conclusions

Observations from a variety of ground-based remote sensors, combined with visible satellite imagery and documentation of trapped mountain lee waves in previous studies, were used to demonstrate that these waves can undergo significant changes in wavelength on a timescale of roughly 1 h. In one case study, with particularly accurate measurements of nonstationarity based on Doppler lidar data, it was shown that the wavelength increased rather steadily by 6% h^{-1} over 3.7 h. Visible satellite images from 15 other events also revealed wavelength increases of this magnitude and larger. By combining these newly documented cases with those already in the literature, 24 events were identified in which a temporal wavelength change was clearly

TABLE 3. Summary of observations of trapped lee-wave nonstationarity.

Date	Average wavelength (km)	Number of wavelengths	Time (h) over which observations made (UTC)	Rate of change of wavelength (km h^{-1})	Rate of change of wavelength (% h^{-1})
28 Jan 67[a]	11.5	4	1.4 (1903–2027)	0.7	6
30 Jan 67[a]	13.8	3	1.5 (2335–0106)	−0.3	−2
31 Jan 67[a]	15.2	3–5	1.3 (0106–0225)	2.3	15
1 Mar 67[b]	16.0	3	2.0 (1845–2045)	1.5	9
1 Mar 67[c]	19.2	2	1.3 (1840–2000)	2.6	14
3 Feb 70[d]	26.0	1	2.3 (1300–1520)	2.6	10
27 Apr 76[e]	8.3	15	7.1 (1330–2035)	0.5	6
16 Oct 85[f]	12.7	6	1.0 (1730–1830)	−5.4	−43
2 Feb 87[g]	12.7	3	3.7 (1657–2037)	0.8	6
2 Feb 87	14.8	4–5	2.0 (1930–2130)	1.4	10
8 Apr 92	18.2	3–12	1.5 (1930–2100)	2.3	14
30 Jun 92	28.6	4	2.0 (1730–1930)	3.0	5
4 May 94	12.5	3–4	2.0 (2002–2202)	3.4	28
14 Sep 94	12.1	5–6	3.5 (1430–1800)	0.3	2
14 Oct 94	12.9	4–6	2.5 (1900–2130)	1.8	15
21 Oct 94 (western)	15.6	2–5	2.5 (1630–1900)	1.6	10
21 Oct 94 (eastern)	19.1	2	2.0 (1630–1830)	2.7	14
1 Dec 94	15.9	3–4	2.0 (2130–2330)	1.0	6
2 Dec 94	14.2	5	3.5 (1900–2230)	0.6	4
4 Dec 94 (northern Colorado)	14.4	3–6	2.0 (2030–2230)	1.3	9
4 Dec 94 (central Colorado)	13.4	3–4	0.5 (2030–2100)	3.8	28
12 Feb 95 (early)	17.4	3–4	2.0 (1630–1830)	−0.2	−1
12 Feb 95 (late)	19.4	3–4	2.0 (1930–2130)	2.5	13
29 Mar 96 (Oregon)	14.0	4	3.8 (1445–1830)	−1.4	−10
Average	15.8 ± 4.5	4	2.3	1.5 ± 1.3	9.2 ± 8.5

[a] From constant-volume balloons in Colorado (Vergeiner and Lilly 1970).
[b] From aircraft in Colorado (Vergeiner and Lilly 1970).
[c] From ruby lidar in California (Collis et al. 1968).
[d] From 10-cm-wavelength radar in England (Starr and Browning 1972).
[e] From visible satellite images (Weiss 1976).
[f] From satellite image near Macquarie Island at about 160°E (Mitchell et al. 1990).
[g] From CO_2 Doppler lidar in Colorado (this study).
All others are from visible satellite images of the Rocky Mountains (this study).

measured. On average, the wavelength increased by 9.2% h^{-1}, or 1.5 km h^{-1}, with extreme values exceeding 25% h^{-1} and 3 km h^{-1}. In one case it was estimated that the wavelength decreased very rapidly at 43% h^{-1}. Although the approach taken here cannot determine what fraction of all trapped lee waves exhibits nonstationarity, and what the average magnitude of temporal change is, it is worth noting the clear tendency for wavelengths to increase with time in the sample studied. Future efforts could systematically determine the average rate of wavelength change of all trapped lee-wave clouds observed by visible satellite over a limited area during an extended period of time. Because most of the events were observed during the day, except for two of the four for which wavelength decreased with time, the statistics best represent behavior characteristic of the daylight portion of the diurnal cycle.

It was shown using a detailed case study of 8 April 1992 that the wavelength change in one event was primarily a result of changing upstream conditions. This was accomplished through the analysis of hourly wind and temperature profiles from RASS and wind profilers, which clearly documented significant temporal changes over roughly 3–4 h in the strength, thickness, and height of both the key stable layer and the shear layer. These data were then used to initialize a two-dimensional, nonhydrostatic numerical model that has been used extensively to study both trapped and vertically propagating mountain waves (Pihos and Wurtele 1981; Sharman et al. 1988). Several simulations were performed, each using initial conditions from a different time. The simulations showed an overall temporal increase in wavelength roughly in accord with observations, except that the predicted wavelengths were systematically too short. This bias likely resulted from a spurious broadening of the stable layer thickness due to the coarse vertical resolution of the data. Such a tendency should be anticipated from theoretical results (Corby and Wallington 1956), which showed that the trapped wavelength is inversely related to the stable layer thickness. Three possible mechanisms were suggested that were likely involved in modifying the wave environment of this case: 1) a passing baroclinic disturbance that affected the strength and altitude of a frontal zone containing strong stratification and vertical shear that were important in determining the trapped wave response, 2) the

upward erosion of the primary elevated stable layer near 4 km MSL by a deepening convective boundary layer in the lee of the mountains, and 3) changes in the forcing due to diurnal changes in the boundary layer over the mountains. Although the third mechanism was likely active, it was not observable in this study. However, both mechanisms 1 and 2 were clearly documented. The fact that the limited climatology shows a strong bias toward temporally increasing wavelength during the day makes it likely that mechanism 2 is dominant in many cases, although certainly changes in frontal characteristics will dominate in some events and in locations where the diurnal cycle may not be as important, such as over the oceans.

This study also establishes that the RASS, wind profiler, and lidar that were used had enough accuracy and temporal resolution to provide unique information on mountain wave nonstationarity. In particular, the RASS and wind data were accurate enough to document changes in the wave environment that were responsible for changes in the trapped wavelength. It was also shown that errors in the predicted wavelength based on using measurements from within the trapped lee waves, rather than upstream data, were small compared to the observed rate of wavelength change. Although it had been recognized that large (>1 m s^{-1}) and temporally variable vertical velocities observed by wind profilers in the lee of mountains resulted from mountain waves, this study presents the first observations made when trapped lee waves were unambiguously present. Unlike the earlier study by Ralph et al. (1992), in which an extended period dominated by trapped lee waves in the lee of a small mountain was revealed by vertical profiles of wind profiler–observed vertical velocities, this study used the same technique to show that both vertically propagating and trapped modes were simultaneously present in the lee of the Rockies. This result may be expected based on the relative scales of the mountains. In addition, the Doppler lidar provided especially detailed documentation of the structure of a trapped lee wave, including the relationship between the wave clouds and wave motions, which were observed simultaneously.

Although trapped lee waves are the focus of this study, the implications concerning the rate at which mountain waves change structure are applicable to other types of mountain waves. Observations of temporal changes between trapped and vertically propagating modes over a few hours presented here and in Ralph et al. (1992) support this inference, as do lidar observations of significant temporal changes in a breaking mountain wave over 2 h (Ralph et al. 1997). These results lead to the conclusion that earlier studies of mountain wave drag, which were forced to assume that conditions were stationary over 2–5 h (Lilly and Kennedy 1973; Lilly et al. 1982; Brown 1983; Hoinka 1985; Pitts and Lyons 1989; Hoinka and Clark 1991; Satomura and Bougeault 1994), were susceptible to errors associated with significant changes in the mountain wave structure on those timescales. For example, the uncertainty about stationarity led Lilly and Zipser (1972) to show that the exact position of the upper-tropospheric portion of a large-amplitude mountain wave relative to the lower portion remained ambiguous. This uncertainty may be partly responsible for some of the important disparities remaining between observed and simulated mountain wave drag, as has been suggested by Hoinka and Clark (1991), and Satomura and Bougeault (1994). The observational capabilities illustrated in this study should allow future mountain wave studies to begin addressing the important issue of mountain wave evolution. These techniques may be useful in identifying time intervals over which the conditions are sufficiently stationary for the wave drag to be derived from aircraft measurements without undue errors resulting from temporal changes in wave structure.

Acknowledgments. This study benefitted from the availability of data from a variety of remote sensors operated in the vicinity of Colorado's Front Range. The efforts of many people in maintaining these instruments and making the data available are recognized, especially Dr. Richard Strauch and Bob Weber for their assistance with the 50-MHz profiler and RASS data. The NOAA Forecast Systems Laboratory is gratefully acknowledged for supporting the real-time data display and review system that allowed identification and measurement from visible satellite data of the many trapped lee wave cloud events used in this study. The 1996 event in Oregon was pointed out by Louisa Nance. Comments from John Brown, Tom Schlatter, and Louisa Nance helped refine the text, as did reviews by Andrew Crook, Ross Mitchell, and an anonymous reviewer. Expert drafting and preparation of figures by Jim Adams is greatly appreciated, as is the preparation of tables by Karen Martin.

APPENDIX

Errors Due to Using Measurements from within the Trapped Lee Waves Rather than Upstream to Initialize the Numerical Model

The wind profiler and RASS data, used to define the initial conditions for the simulations of the 8 April 1992 case, were observed downstream of the mountains and thus represent the combination of both the background state and the wave perturbations. Because of this, the assumption used here that these observations represent upstream conditions may introduce significant errors in the simulated waves when trying to compare them with the observed waves. In order to assess the importance of this uncertainty in the 8 April 1992 case the simulation initialized with data from 1730 UTC is examined in more detail. Figure A1 shows the simulated vertical velocities and density within the trapped waves 100 min into the

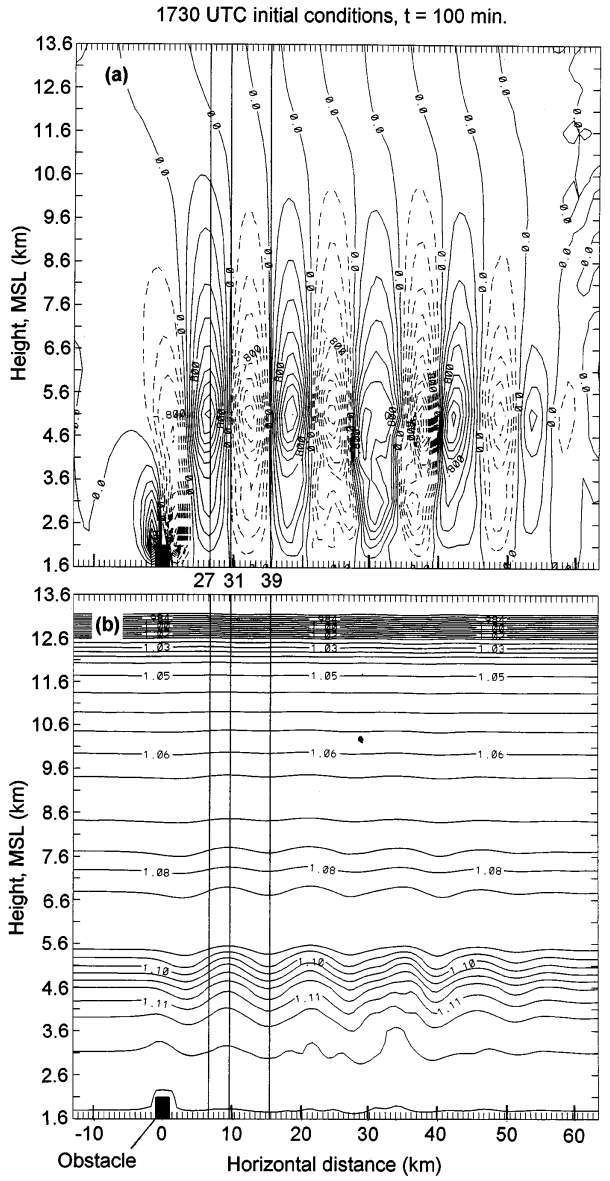

FIG. A1. (a) Upward (solid) and downward (dashed) vertical motion contoured every 0.2 m s^{-1} from 100 min into the simulation initialized using data from 1730 UTC 8 April 1992. (b) Same as in (a), but for the Boussinesq version of density used by the model (magnitudes are labeled, but only the vertical gradient is used). The contours in (b) can also be interpreted as streamlines or isentropes because conditions are adiabatic. Vertical lines mark the positions from which the vertical profiles shown in Fig. A2 were extracted for the sensitivity test summarized in Table A1. The profiles are labeled by their horizontal grid point (i) position, with $i = 27$ at the position of maximum upward motion, $i = 31$ at the position of maximum upward displacement, and $i = 39$ at the position of maximum downward displacement. Tick marks show grid points.

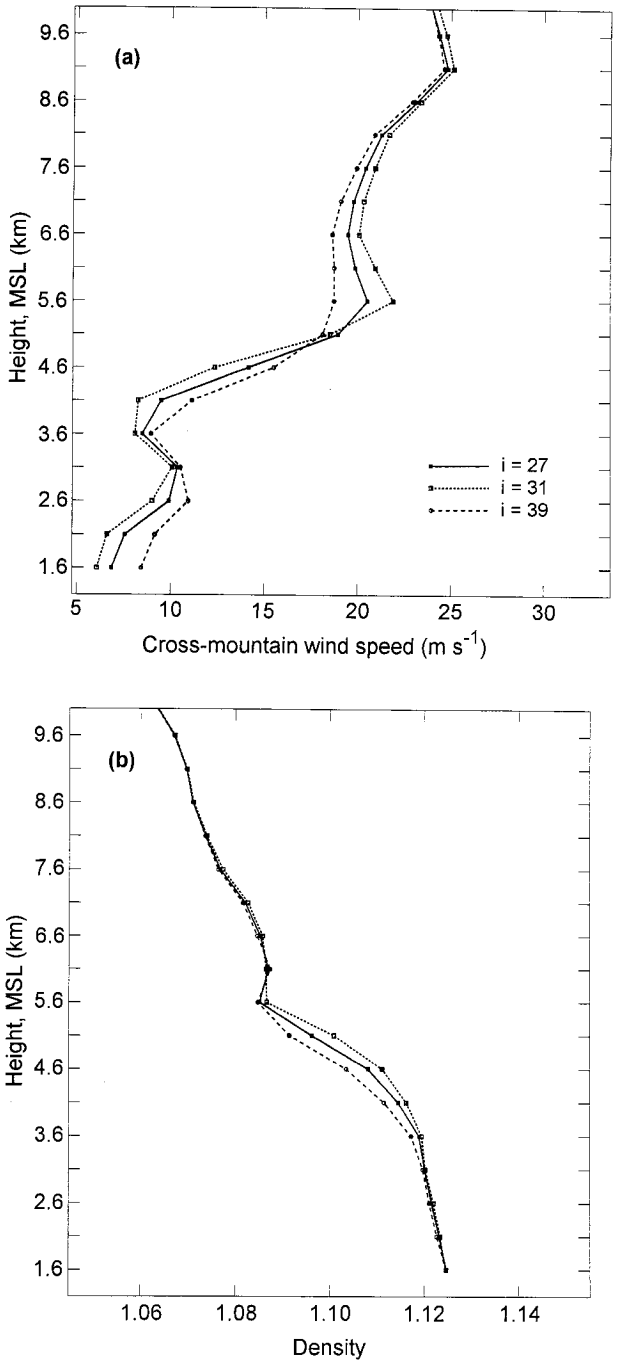

FIG. A2. (a) Vertical profiles of horizontal (cross-mountain) wind (m s^{-1}) and (b) Boussinesq density from the three positions within the simulated wave pattern shown in Fig. A1.

simulation. Profiles of horizontal wind and temperature are taken from this simulation at three key positions from within the wave field, which are marked in Fig. A1. These profiles are shown in Fig. A2 and represent conditions where the upward vertical displacement is greatest, the downward vertical displacement is greatest, and vertical displacement is zero. The first two correspond to the positions where the vertical velocity is zero and the last to where vertical velocity is a maximum.

These three profiles are each used to initialize a separate simulation. The results of these three simulations, and the original simulation using the observed initial

TABLE A1. Uncertainty in simulations due to the presence of wave perturbations in the model initial conditions.

Experiment/position	Horizontal wavelength (km)	Maximum vertical velocity in waves (m s^{-1})	Altitude of maximum vertical velocity (km MSL)
Original 1730 UTC run	12.0	1.9	5.1
Maximum vertical velocity	11.9	1.9	5.1
Maximum upward displacement	12.3	1.5	5.2
Maximum downward displacement	11.6	1.7	4.9
Average ± uncertainty	12.0 ± 0.3	1.7 ± 0.2	5.1 ± 0.1

conditions, are summarized in Table A1. These results show that the simulated wavelength at the altitude of maximum vertical velocity varied from 11.6 to 12.3 km, an uncertainty of approximately ±3% of the total wavelength. This is small compared to the 30% increase in simulated wavelength from 1530 to 2130 UTC, and the 20% increase observed in satellite images between 1930 and 2100 UTC. Both the vertical velocity perturbation amplitude and the altitude of the maximum vertical velocity changed little between these runs, that is, 1.7 ± 0.2 m s^{-1} and 5.1 ± 0.1 km, respectively.

Because the results of this test depend on the amplitude of the perturbations in the original 1730 UTC simulation, it is important that the simulated wave amplitude be close to that of the observed waves. Because of the unique ability of the wind profilers to directly observe vertical motion, and because the vertical motions are due almost entirely to the waves, this variable is ideal for comparison with the model. Comparison of the observed vertical velocities (Fig. 15) and the simulated vertical velocities (Fig. A1) indicate that both had amplitudes of approximately 2 m s^{-1}. Thus, in this case, the use of measurements from within the train of trapped lee waves as upstream conditions for the numerical simulations introduced an uncertainty that is much smaller than the observed change in horizontal wavelength. Although it is unclear that this same conclusion would be true in all trapped lee wave events, it should be noted that the wave amplitude was significant in this event and thus should apply to many cases. However, as wave amplitude increases the errors due to this assumption will increase.

REFERENCES

Atkinson, B. W., 1981: *Mesoscale Atmospheric Circulations.* Academic Press.

Balsley, B. B., and D. A. Carter, 1989: Mountain waves in the tropical Pacific atmosphere: A comparison of vertical wind fluctuations over Pohnpei and Christmas Island using VHF wind profilers. *J. Atmos. Sci.,* **46,** 2698–2715.

Bannon, P. R., and J. A. Zehnder, 1985: Surface pressure and mountain drag for transient airflow over a mountain ridge. *J. Atmos. Sci.,* **42,** 2454–2462.

Banta, R. M., L. D. Olivier, and D. H. Levinson, 1993: Evolution of the Monterey Bay sea-breeze layer as observed by pulsed Doppler lidar. *J. Atmos. Sci.,* **50,** 3959–3982.

Barth, M. F., R. B. Chadwick, and D. W. van de Kamp, 1994: Data processing algorithms used by NOAA's wind profiler demonstration network. *Ann. Geophys.,* **12,** 518–528.

Bell, T. H., 1975: Lee waves in stratified flows with simple harmonic time dependence. *J. Fluid Mech.,* **67,** 705–722.

Blumen, W., and J. E. Hart, 1988: Airborne Doppler lidar windfield measurements of waves in the lee of Mount Shasta. *J. Atmos. Sci.,* **45,** 1571–1583.

Brown, P. R. A., 1983: Aircraft measurements of mountain waves and their associated momentum flux over the British Isles. *Quart. J. Roy. Meteor. Soc.,* **109,** 849–865.

Clark, T. L., W. D. Hall, and R. M. Banta, 1994: Two- and three-dimensional simulations of the 9 January 1989 severe Boulder windstorm: Comparison with observations. *J. Atmos. Sci.,* **51,** 2317–2343.

Collis, R. T. H., F. G. Fernald, and J. E. Alder, 1968: Lidar observations of Sierra-wave conditions. *J. Appl. Meteor.,* **7,** 227–233.

Corby, G. A., and C. E. Wallington, 1956: Airflow over mountains: The lee-wave amplitude. *Quart. J. Roy. Meteor. Soc.,* **82,** 266–274.

Crook, N. A., 1988: Trapping of low-level internal gravity waves. *J. Atmos. Sci.,* **45,** 1533–1541.

Durran, D. R., 1986: Mountain waves. *Mesoscale Meteorology and Forecasting,* P. S. Ray, Ed., Amer. Meteor. Soc., 472–492.

Ecklund, W. L., K. S. Gage, B. B. Balsley, R. G. Strauch, and J. L. Green, 1982: Vertical wind variability observed by VHF radar in the lee of the Colorado Rockies. *Mon. Wea. Rev.,* **110,** 1451–1457.

Foldvik, A., 1962: Two-dimensional mountain waves—A method for the rapid computation of the lee wavelengths and vertical velocities. *Quart. J. Roy. Meteor. Soc.,* **88,** 271–285.

——, and M. G. Wurtele, 1967: The computation of the transient gravity wave. *Geophys. J. Roy. Astron. Soc.,* **13,** 167–185.

Förchtgott, J., 1957: Active turbulent layer downwind of mountain ridges. *Schweiz. Aero-Rev.,* **32,** 324–335.

Gage, K. S., 1990: Radar observations of the free atmosphere: Structure and dynamics. *Radar in Meteorology,* D. Atlas, Ed., Amer. Meteor. Soc., 534–565.

Gerbier, N., and M. Berenger, 1961: Experimental studies of lee waves in the French Alps. *Quart. J. Roy. Meteor. Soc.,* **87,** 13–23.

Heymsfield, A. J., and L. M. Miloshevich, 1995: Relative humidity and temperature influences on cirrus formation and evolution: Observations from wave clouds and FIRE II. *J. Atmos. Sci.,* **52,** 4302–4326.

Hoinka, K. P., 1985: Observation of the airflow over the Alps during a foehn event. *Quart. J. Roy. Meteor. Soc.,* **111,** 199–224.

——, and T. L. Clark, 1991: Pressure drag and momentum fluxes due to the Alps. Part I: Comparison between numerical simulations and observations. *Quart. J. Roy. Meteor. Soc.,* **117,** 495–525.

Holmboe, J., and H. Klieforth, 1957: Investigations of mountain lee waves and airflow over the Sierra Nevada. Final Rep., Contract AF19(604)-728, University of California AD No. 133606, Dept. of Meteorology, University of Califonia, Los Angeles, Los Angeles, CA, 290 pp.

Keller, T. L., 1994: Implications of the hydrostatic assumption on atmospheric gravity waves. *J. Atmos. Sci.,* **51,** 1915–1929.

Kuettner, J., 1959: The rotor in the lee of mountains. Geophysics Research Directorate GRD Note 6, AD-208862, Air Force Cambridge Research Laboratories, Bedford, MA 20 pp.

Larsen, M. F., and J. Röttger, 1991: VHF radar measurements of in-beam incidence angles and associated vertical-beam radial velocity corrections. *J. Atmos. Oceanic Technol.,* **8,** 477–490.

Lilly, D. K., 1983: Linear theory of internal gravity waves and mountain waves. *Mesoscale Meteorology Theories, Observations, and Mod-*

els, D. K. Lilly and T. Gal-Chen, Eds., D. Reidel Publishing, 293–312.

——, and E. J. Zipser, 1972: The Front Range windstorm of 11 January 1972—A meteorological narrative. *Weatherwise,* **25,** 56–63.

——, and P. J. Kennedy, 1973: Observations of a stationary mountain wave and its associated momentum flux and energy dissipation. *J. Atmos. Sci.,* **30,** 1135–1152.

——, J. M. Nicholls, R. M. Chervis, P. J. Kennedy, and J. B. Klemp, 1982: Aircraft measurements of wave momentum flux over the Colorado Rocky Mountains. *Quart. J. Roy. Meteor. Soc.,* **108,** 625–642.

Long, R. R., 1955: Some aspects of the flow of stratified fluids. III: Continuous density gradients. *Tellus,* **7,** 341–357.

Lott, F., and H. Teitelbaum, 1993: Topographic waves generated by a transient wind. *J. Atmos. Sci.,* **50,** 2607–2624.

May, P. T., R. G. Strauch, K. P. Moran, and W. L. Ecklund, 1990: Temperature sounding by RASS with wind profiler radars: A preliminary study. *IEEE Trans. Geosci. Remote Sens.,* **28,** 19–28.

McAfee, J. R., R. G. Strauch, and K. S. Gage, 1994: Examples of vertical velocity comparison from collocated VHF and UHF profilers. *Radio Sci.,* **29,** 879–880.

Mitchell, R. M., R. P. Cechet, P. J. Turner, and C. C. Elsum, 1990: Observation and interpretation of wave clouds over Macquarie Island. *Quart. J. Roy. Meteor. Soc.,* **116,** 741–752.

Mohr, C. G., L. J. Miller, R. L. Vaughn, and H. W. Frank, 1986: Merger of mesoscale datasets into a common Cartesian format for efficient and systematic analysis. *J. Atmos. Oceanic Technol.,* **3,** 143–161.

Moran, K. P., and R. G. Strauch, 1994: The accuracy of RASS temperature measurements corrected for vertical air motion. *J. Atmos. Oceanic Technol.,* **11,** 995–1001.

Neiman, P. J., R. M. Hardesty, M. A. Shapiro, and R. E. Cupp, 1988: Doppler lidar observations of a downslope windstorm. *Mon. Wea. Rev.,* **116,** 2265–2275.

——, P. T. May, and M. A. Shapiro, 1992: Radio acoustic sounding system (RASS) and wind profiler observations of lower- and mid-tropospheric weather systems. *Mon. Wea. Rev.,* **120,** 2298–2313.

Palm, E., and A. Foldvik, 1960: Contribution to the theory of two-dimensional mountain waves. *Geofys. Publ.,* **21,** 1–30.

Pihos, G. G., and M. G. Wurtele, 1981: An efficient code for the simulation of non-hydrostatic flow over obstacles. NASA CR 3385. [NTIS N81-23762.]

Pitts, R. O., and T. J. Lyons, 1989: Airflow over a two-dimensional escarpment. Part I: Observations. *Quart. J. Roy. Meteor. Soc.,* **115,** 965–981.

Post, M. J., and R. E. Cupp, 1990: Optimizing a pulsed Doppler lidar. *Appl. Opt.,* **29,** 4145–4158.

Prichard, I. T., L. Thomas, and R. M. Worthington, 1995: The characteristics of mountain waves observed by radar near the west coast of Wales. *Ann. Geophys.,* **13,** 757–767.

Queney, P., 1948: The problem of airflow over mountains: A summary of theoretical studies. *Bull. Amer. Meteor. Soc.,* **29,** 16–26.

——, G. A. Corby, N. Gerbier, H. Koschmieder, and J. Zierep, 1960: The airflow over mountains. WMO Tech. Note 34, World Meterological Organization, Geneva, Switzerland, 135 pp.

Ralph, F. M., 1991: Mesoscale studies using clear-air Doppler radar. Ph.D. thesis, University of California, 177 pp. [Available from Universal Microfilms International, 300 N. Zeeb Road, Ann Arbor, MI 48106.]

——, 1995: Using radar-measured radial vertical velocities to distinguish precipitation scattering from clear-air scattering. *J. Atmos. Oceanic Technol.,* **12,** 257–267.

——, M. Crochet, and S. V. Venkateswaran, 1992: A study of mountain lee waves using clear-air radar. *Quart. J. Roy. Meteor. Soc.,* **118,** 597–627.

——, P. J. Neiman, D. W. van de Kamp, and D. C. Law, 1995: Using spectral moment data from NOAA's 404-MHz radar wind profilers to observe precipitation. *Bull. Amer. Meteor. Soc.,* **76,** 1717–1739.

——, ——, and D. Levinson, 1997: Lidar observations of a breaking mountain wave associated with extreme turbulence. *Geophys. Res. Lett.,* in press.

Reynolds, R. D., R. L. Lamberth, and M. G. Wurtele, 1968: Investigation of a complex mountain wave situation. *J. Appl. Meteor.,* **7,** 353–358.

Sato, K., 1990: Vertical wind disturbances in the troposphere and lower stratosphere observed by the MU radar. *J. Atmos. Sci.,* **47,** 2803–2817.

Satomura, T., and P. Bougeault, 1994: Numerical simulations of lee wave events over the Pyrenees. *J. Meteor. Soc. Japan,* **72,** 173–195.

Sawyer, J. S., 1962: Gravity waves in the atmosphere as a three-dimensional problem. *Quart. J. Roy. Meteor. Soc.,* **88,** 412–425.

Scorer, R. S., 1949: Theory of lee waves of mountains. *Quart. J. Roy. Meteor. Soc.,* **75,** 41–56.

Sharman, R. D., and M. G. Wurtele, 1983: Ship waves and lee waves. *J. Atmos. Sci.,* **40,** 418–427.

——, T. L. Keller, and M. G. Wurtele, 1988: Incompressible and anelastic flow simulations on numerically generated grids. *Mon. Wea. Rev.,* **116,** 1124–1136.

Shaw, J. A., and L. S. Fedor, 1992: Improved calibration of infrared radiometers for cloud-temperature remote sensing. *Opt. Eng.,* **32,** 1002–1010.

Shutts, G. J., and A. Broad, 1993: A case study of lee waves over the Lake District in northern England. *Quart. J. Roy. Meteor. Soc.,* **119,** 377–408.

Smith, R. B., 1979: The influence of mountains on the atmosphere. *Advances in Geophysics,* Vol. 21, Academic Press, 87–230.

——, and J. Sun, 1987: Generalized hydraulic solutions pertaining to severe downslope winds. *J. Atmos. Sci.,* **44,** 2934–2939.

Starr, J. R., and K. A. Browning, 1972: Observations of lee waves by high-power radar. *Quart. J. Roy. Meteor. Soc.,* **98,** 73–85.

Strauch, R. G., B. L. Weber, A. S. Frisch, C. G. Little, D. A. Merritt, K. P. Moran, and D. C. Welsh, 1987: The precision and relative accuracy of profiler wind measurements. *J. Atmos. Oceanic Technol.,* **4,** 563–571.

van Baelen, J. S., A. D. Richmond, T. Tsuda, S. K. Avery, S. Kato, S. Fukao, and M. Yamamoto, 1991: Radar interferometry technique and anisotropy of the echo power distribution: First results. *Radio Sci.,* **26,** 1315–1326.

Vergeiner, I., and D. K. Lilly, 1970: The dynamic structure of lee wave flow as obtained from balloon and airplane observations. *Mon. Wea. Rev.,* **98,** 220–232.

Viezee, W., R. T. H. Collis, and J. D. Lawrence, 1973: An investigation of mountain waves with lidar observations. *J. Appl. Meteor.,* **12,** 140–148.

Weiss, C. E., 1976: Diurnal variation in the wavelength of lee standing waves. NOAA/National Weather Service/National Environmental Satellite Service, Satellite Applications Information Note 76/14, NOAA–S/T 76-2404, National Environmental Satellite Service, Washington, DC, 7 pp.

Worthington, R. M., and L. Thomas, 1996: Radar measurements of critical-layer absorption in mountain waves. *Quart. J. Roy. Meteor. Soc.,* **122,** 1263–1282.

Wuertz, D. B., B. L. Weber, R. G. Strauch, A. S. Frisch, C. G. Little, D. A. Merritt, K. P. Moran, and D. C. Welsh, 1988: Effects of precipitation on UHF wind profiler measurements. *J. Atmos. Oceanic Technol.,* **5,** 450–465.

Wurtele, M. G., R. D. Sharman, and T. L. Keller, 1987: Analysis and simulations of a troposphere–stratosphere gravity wave model. Part I. *J. Atmos. Sci.,* **44,** 3269–3281.

——, ——, and A. Datta, 1996: Atmospheric lee waves. *Annu. Rev. Fluid Mech.,* **28,** 429–476.